International Journal of Mechanical Sciences 242 (2023) 108031

Contents lists available at ScienceDirect

International Journal of Mechanical Sciences

journal homepage: www.elsevier.com/locate/ijmecsci

Cutting mechanics and efficiency of forward and reverse multidirectional turning

Wei Cai [a,b,c,*], Yuanhui Zhang [a], Li Li [a], Tao Peng [d], Kee-hung Lai [b], Marian Wiercigroch [e,**]

[a] College of Engineering and Technology, Southwest University, Chongqing 400715, China
[b] Department of Logistics and Maritime Studies, The Hong Kong Polytechnic University, Hung Hum, Kowloon, Hong Kong, China
[c] Yibin Academy of Southwest University, Yibin, Sichuan 644000, China
[d] State Key Laboratory of Fluid Power and Mechatronic Systems, School of Mechanical Engineering, Zhejiang University, Hangzhou 310027, China
[e] Centre for Applied Dynamics Research, School of Engineering, King's College, University of Aberdeen, Fraser Noble Building, Aberdeen, Scotland AB24 3UE, UK

ARTICLE INFO

Keywords:
Cutting mechanics
Cutting force and temperature
Stress in cutting zone
Chip formation
Multidirectional turning (MDT)

ABSTRACT

In the manufacturing industry, many studies have been conducted on the features of cutting force, temperature and chip that are directly related to tool wear and cutting performance. However, most of the leading investigations have focused on unidirectional cutting and relatively few on multidirectional cutting. This study proposes a new approach to one of the most popular cutting operation of turning, in the form of forward-and-reverse multidirectional turning (MDT) to overcome deficiencies of tool wear, low processing efficiency and chip breakage using conventional turning. The mechanism and fundamentals of MDT are illustrated through dynamics analysis. A thermomechanical coupling simulation model is established in ABAQUS to analyze the mechanical properties of MDT. Three machining schemes are created with tool cutting edge angles as variables, and the optimal machining scheme is selected by analyzing features of cutting force, temperature, stress and chip morphology. Furthermore, the smaller-the-better characteristic of Taguchi's method and signal-to-noise ratio are used to analyze the effect of cutting parameters on the MDT performance. Finally, a case study illustrates practicability of the proposed approach is verified by the experimental studies.

1. Introduction

Cutting operations that are widely used to machine various types of parts play an important role in the manufacturing industry [1,2]. With the emergence of the next generation of information technology, industrial internet, big data, cutting processing towards intelligent, automated and sustainable development aiming at high quality and efficiency [3]. Manufacturers and toolmakers are constantly developing new machines and tools with novel information technology and manufacturing technology to improve their competitiveness [4,5]. For the cutting process and turning in particular, although it has a long history, the tool wear and chip tangling, processing efficiency and other issues for turning have been plaguing producers and operating workers [6,7]. Therefore, it is crucial to establish a machining approach that to solve these multiple challenges.

Many scholars have contributed to development of cutting from various theories and approaches. Regarding cutting force, Fu et al. [8] showed that cutting forces have a significant impact on tool wear and breakage, machine vibration and power. There is a growing demand to reduce tact time by reducing cutting forces and extending the life of tools [9]. Cutting force characteristics in laser-coated remanufactured turning were investigated. Uneven contours tend to lead to tool breakage during rough turning, while cutting vibration has a significant effect on the radial force component during finishing turning [10]. The anti-friction properties of the bionic microstructure rake surface tools were investigated in dry cutting of Ti6Al4V. The bionic surface can effectively reduce the cutting force and improve the cutting performance in certain cutting speed ranges [11]. The effects of cutting speed, feed rate and depth of cut on surface roughness and tangential cutting forces were investigated in dry turning of Inconel 718 with ceramic and cemented carbide tools [12]. The analysis of variance calculation showed that vibration frequency was the main factor affecting cutting force and vibration amplitude was the main factor affecting temperature [13]. By studying hard turning of GCr15 bearing steel. It was found that

* Corresponding author address: College of Engineering and Technology, Southwest University, Chongqing 400715, China.
** Corresponding author.
E-mail addresses: weicai@swu.edu.cn (W. Cai), m.wiercigro@abdn.ac.uk (M. Wiercigroch).

https://doi.org/10.1016/j.ijmecsci.2022.108031
Received 26 October 2022; Received in revised form 8 December 2022; Accepted 10 December 2022
Available online 11 December 2022

the effect of feed rate on cutting forces and surface roughness is greater than that of cutting speed, and that there exists an optimum cutting speed that produces minimum surface roughness with relatively small cutting forces [14]. The effect of cutting parameters on the force components was studied by developing an elastic element sensitive to torsion and bending. The results show that the three components of the cutting force decrease with increasing cutting speed and increase linearly with feed rate and depth of cut, and the effect of cutting speed on the three components is not significant [15]. Cutting speed on cutting forces and chip shrinkage during turning of titanium alloy BT6 was determined experimentally. Light feeds and high cutting speeds are not recommended for safe operations [16]. Besides, the effect of different cutting parameters on cutting force and surface roughness of A100 steel and 300 M steel was studied by orthogonal test method to improve the turning performance of ultra-high strength steel for aircraft landing gear [17].

Regarding cutting temperature, Shah et al. [18] pointed out that high cutting temperature is a serious problem that needs to be addressed because, it results in poor machinability. The high specific pressure and high temperature in the cutting zone leads to a decrease in the hardness of the tool material, increased wear and deformation of the cutting elements, loss of cutting ability, and ultimately to the failure of the tool [19]. The contact phenomena and temperature field of carbide tools for finishing VT1-0 titanium alloy were studied, and the dependence of cutting speed on temperature variation was determined [20]. The effects of cutting speed, feeding, depth of cut and workpiece hardness on the cutting temperature at the tool-workpiece interface during hard turning of American Iron and Steel Institute (AISI) H13 tool steel parts were investigated [21]. By analyzing tool wear experiments, it is evident that tool wear rate increases with cutting temperature [22]. Relative higher cutting temperatures produced thermal softening effects, making the tool more susceptible to wear or breakage [23]. By considering the problems associated with high cutting temperature and high bonding at the tool working interface for titanium alloy machining, the optimal parameters for the best cutting conditions were obtained [24]. The cutting temperatures of turning super duplex stainless steel (SDSS) under dry cutting, wet cutting and air-cooled cutting conditions were investigated, and it was concluded that air-cooled machining has better cutting performance [25]. The characteristics of cutting zone temperature when turning aluminum alloy with carbide inserts was studied and the results show that the feed and the nose radius are the main factors affecting the cutting zone temperature [26].

Regarding cutting chip formations, Wu et al. [27] pointed out that the cutting chips broken at an appropriate length was an important condition for improving production efficiency and realizing automatic production. Chip morphology was one of the indicators to evaluate the cutting performance of the tool. The chip forming process has a direct and important influence on the chip morphology [28]. The chip forms characteristics obtained from cutting tests under different cutting conditions were analyzed and compared, and the influence of cutting parameters on the force, temperature and stress on the shear surface was revealed [29]. Under high cutting forces, chip formation mechanism, chip morphology and microstructure in the cutting process were analyzed [30]. The cutting parameters affect the characteristics of serrated chips during high-speed machining of nickel-based alloys through observing chip metallographs [31]. The types and variations of chips were introduced, and the chip formation mechanism of ultrasonic vibration-assisted turning was studied and analyzed in [32]. By investigating chip formation and turning chatter during dry turning of high temperature alloy GH4169, the deformation process of the serrated chips under the conditions of low cutting speed and high feed rate was observed [33]. Moreover, the Finite Element Method (FEM) was used to simulate harmonic spindle speed variation and constant speed to reveal the chip formation mechanism during Ti6AI4V machining [34].

Meanwhile, the process of cutting is a complex process, involving elasto-plastic mechanics, fracture mechanics and other disciplines [35]. The stress distribution, strain distribution and cutting temperature distribution of each deformation zone in the turning region cannot be solved satisfactorily by the numerical solution method [36]. Hence, FEM has been used extensively to study cutting performance by leading researchers [37]. For example, FEM based studies were used for aluminum alloy cutting research and some scholars conclude that finite element analysis can effectively replace experimental research [38]. Cutting forces and chip morphology of cutting cylindrical materials were investigated. The cutting forces and chip morphologies obtained from finite element simulations are in a good agreement with experimental results [39]. For example, an orthogonal cutting finite element model was established in ABAQUS, and the effects of cutting parameters on the performance of machined parts and their interactions were analyzed using ANOVA [40]. Similarly, a finite element model was established by ABAQUS to obtain the cutting force, chip formation and cutting temperature distribution of TC21 alloy during the cutting process [41]. The formation process of chips in AISI 4140 cutting and the process forces generated were investigated through 2D model and 3D model FEM simulations. The deviation between 2D simulation results and experimental results is within 20%, while 3D simulation produces similar results but tends to overestimate the cutting forces [42]. The effects of cutting parameters on machining of SiCPAI7075 composites in terms of cutting force and cutting temperature were investigated by FEM in [43]. Also, a FE model of orthogonal cutting was developed to investigate the effects of hard turning parameters on the performance of machined parts [44]. The results of many researches also verify the feasibility of using Finite Element Method to study cutting machining [44,45].

Based on a wide range of existing studies looking at the mechanics of the cutting processes and its characteristics and efficiency, the following research gaps have been identified:

- Most of the past studies have centered on unidirectional cutting, and investigation of multidirectional cutting is urgently needed to address the conflict between tool wear and processing efficiency.
- Many findings have been obtained by studying cutting forces and temperatures, chip formations for unidirectional cutting, but investigations of these features for multidirectional cutting to improve cutting performance are yet to be carried out.

To fill these gaps in knowledge, a new approach of forward-and-reverse multidirectional cutting (MDC) was proposed, contributing to reducing tool wear, alleviating chip tangling and improving processing efficiency. Cutting mechanism of MDC will be revealed by fundamentals and mechanical characteristics analysis. The MDC thermomechanical coupling model is established in ABAQUS 2017, and the MDC scheme to determine optimal performance will be based on the analysis of cutting force and temperature, cutting stress and chip formation and breakage as evaluation indexes. The effect of cutting parameters on the performance of MDC and tool wear distribution will be investigated by orthogonal experiments. The results will show that MDC is promising and the 3D simulation model can well reflect the mechanical characteristics of MDC.

From the theoretical perspective, the cutting mechanism of MDC in form of MDT will be revealed, and the influence variables of MDC will be established. A method to enhance the cutting performance and practical applications of MDC will be discussed. The kinetics and thermodynamics of MDC are analyzed by building a simulation model of MDC and experimental studies. FEM analysis was combined with multidirectional cutting to investigate the effect of tool parameters on the cutting performance of MDC. From a practical perspective, a novel approach of cutting machining with more material removal potential than conventional unidirectional cutting will be presented. Parameter recommendations are given to reduce tool wear. which provides a theoretical basis and methodological guidance for expanding the application of MDC in manufacturing. Meanwhile, it provides a reference for the study of cutting performance using finite element 3D simulation. The application

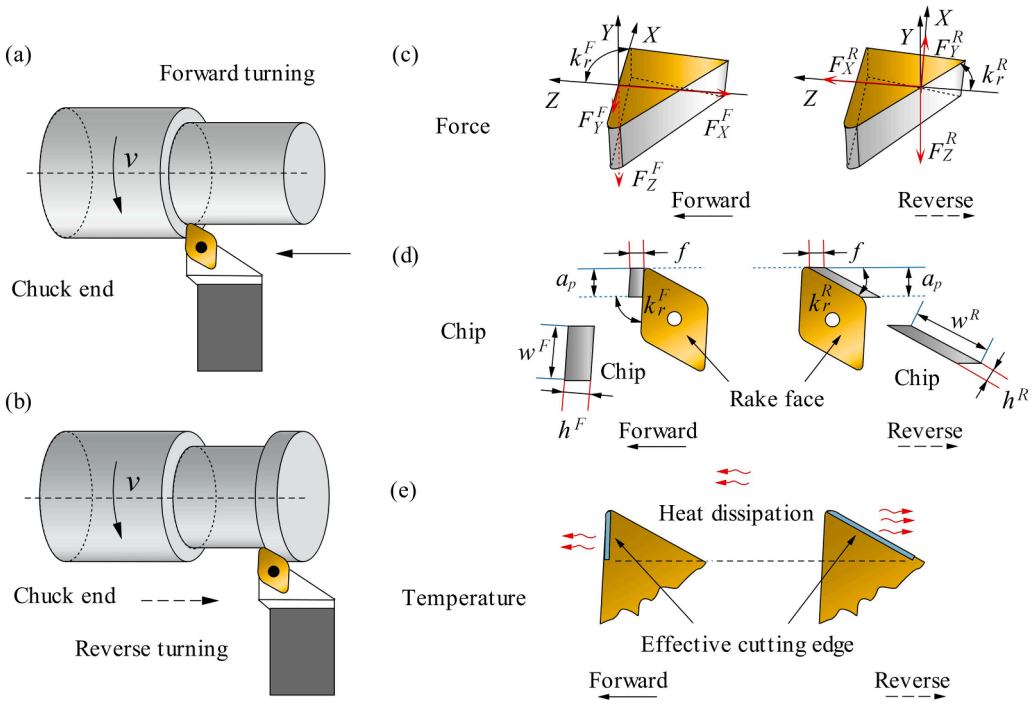

Fig. 1. Schematics of the MDC machining fundamentals. (a) Direction of MDT forward turning facing the chuck; (b) direction of the MDT reverse turning away from the chuck. The MDT forward turning uses the tool cutting edge angle for machining while reverse turning uses the end cutting edge angle. Differences in (c) triaxial force, (d) chip morphology and (e) heat dissipation between forward turning and reverse turning, caused by variety of cutting tool angles.

of the finite element method to multidirectional cutting is conducive to saving consumables and improving efficiency.

The structure of this paper is as follows. In Section 2, the fundamentals of MDC and the influence mechanism of mechanical properties are presented. Section 3 introduces the simulation flow considering MDC multi-features. In Section 4, the MDC cutting performance was verified and analyzed by orthogonal experiments, and finally some conclusions have been drawn.

2. Fundamentals of forward-and-reverse multidirectional cutting

In a conventional unidirectional cutting process, an idling stage when the tool moves but there is no material removal, is inevitable and the energy consumption for this stage can be significant [46]. Multi-tool and multidirectional machining are emerging and developing in the mechanical industry [47,48]. Multidirectional cutting has a major advantage in reduction of tool idle energy consumption. Nevertheless, the use of multidirectional cutting lacks scientific guidance and theoretical support. Based on this context, this paper proposes forward-and-reverse multidirectional cutting (MDC) approach contributing to providing higher material removal efficiency, economic and environmental benefits. The MDC refers to achieve the multidirectional material removal for cutting operation with one tool, and the tool retraction process of the conventional cutting is replaced by reverse cutting of the MDC. The tool idling process is reduced, providing the new opportunity for manufacturers to improve machine and reduce energy consumption. The forward cutting and reverse cutting processes of the MDT are shown in Fig. 1(a) and 1(b), respectively. When machining the excircle of a cylindrical bar, the feeding direction of the tool faces the chuck during forward turning, and the tool feeding direction is away from the chuck when reverse turning. The change of the feeding direction of the MDT causes the contact conditions between the tool and the workpiece to change, resulting in differences in the turning process mechanics.

When the tool tip radius is constant, the change of the assembly position of the tool and the workpiece can cause the corresponding change of the tool cutting edge angle and the end cutting edge angle. The tool cutting edge angle of reverse turning is the end cutting edge angle of forward turning, defined as reverse tool cutting edge angle. Besides, the tool cutting edge angle of the tool is greater than 90° to prevent an interference when reverse turning the end face. The cutting forces acting on the tool in different cutting processes are shown in Fig. 1(c). The change of the actual tool cutting edge can lead to the change of the tangential force and can affect the proportion of radial force and axial force. This scenario can cause different performance in cutting temperature, tool wear and machine power consumption and so on. The chip morphology during forward and reverse turning is shown in Fig. 1 (d). Under the same cutting parameters, the chip morphology can also change due to the change of the actual tool cutting edge angle. This affects the differences in chip breakage and workpiece surface integrity. The effective cutting edges for forward and reverse turning are shown in the Fig. 1(e). Under the same depth of cut, the effective cutting edge of the tool could be enlarged in reverse turning which affects the cutting heat dissipation. The effective cutting edge of the tool differs between different turning processes resulting in alleviation of the tool wear.

In actual cutting, processing efficiency, cutting power, tool wear, workpiece surface integrity and other performance need to be considered comprehensively [49,50]. High cutting temperature is the main cause of tool wear, resulting in machined surface having residual stress and other defects [51,52]. Cutting force is the main factor affecting machine power and chatter, which is indirectly affecting the surface roughness of the workpiece [53,54]. Chip morphology and its breakage are vital factors affecting machining stability [55]. Therefore, it is necessary to identify the MDC machining solution that is conducive to reducing cutting temperature, cutting force and improving chip breaking capacity, thus improving its cutting performance [56]. The specific differences in cutting force, chip morphology and cutting temperature between the forward and reverse turning processes are analyzed and discussed in the subsequent simulations and experiments.

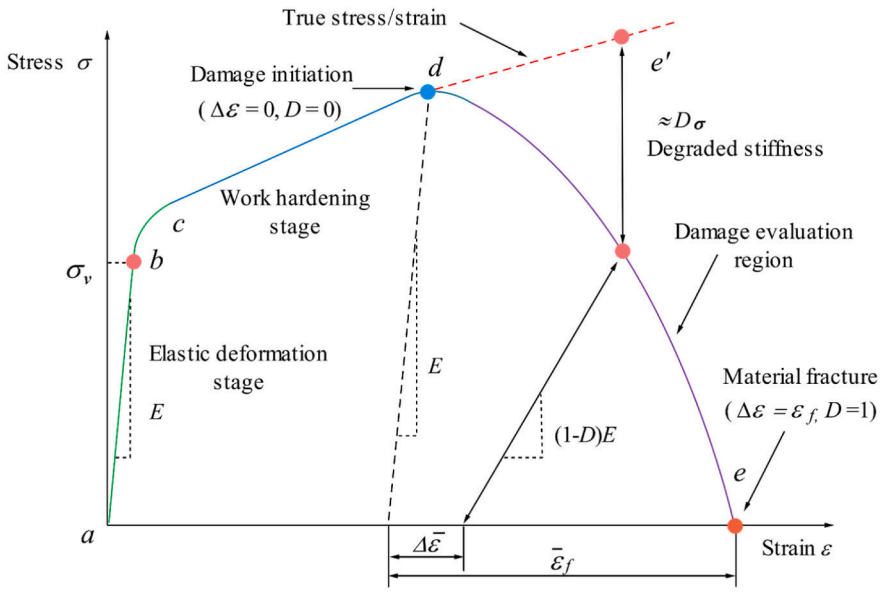

Fig. 2. Stress-strain relation for plastic materials (Abaqus/Explicit). Stage a-b are the linear elastic stage, and stage b-c are the plastic yielding with strain response. When the stress increases and exceeds the yield stress, the material enters the stable plastic deformation stage c-d. Plastic instability starts when the damage parameter (D) is equal to zero (at point d). At point e, the stiffness of the material is completely degraded and the crack initiates as an indication of failure.

3. Cutting force, cutting temperature, chip breakage and cutting stress of the MDT

In this section, the thermomechanical coupled simulation model of the MDT is developed in ABAQUS 2017. Three machining schemes were selected with the tool cutting edge angle and end cutting edge angle as variables. The MDT machining scheme with the optimal cutting performance was obtained by using cutting force, cutting temperature, chip breakage and cutting stress as evaluation indexes.

3.1. Material model

As the world's most widely used metal material, steel and iron has a significant influence on human life and social development [57]. Among them, 45 carbon steel has been widely used in ships, bridges, machinery and other fields due to its excellent mechanical properties [58]. Therefore, 45 carbon steel was chosen to study MDT cutting features in this section.

The intrinsic structure relationship of the material is a reflection of the material properties and is one of the most important factors in the finite element analysis of the cutting process. A variety of dynamic material failure models are available in ABAQUS/CAE. In this study, the Johnson-Cook (JC) material damage model is used, integrating the effects of the strain, temperature and strain rate of the material during cutting. The flow stress in the JC model is expressed by the following equation [59]:

$$\sigma = \underbrace{(A + B\bar{\varepsilon}^n)}_{\text{plastic term}} \underbrace{\left[1 + C\ln\left(\frac{\dot{\varepsilon}}{\dot{\varepsilon}_0}\right)\right]}_{\text{viscosity term}} \underbrace{\left[1 - \left(\frac{T - T_r}{T_m - - - T_r}\right)^m\right]}_{\text{softening term}}, \tag{1}$$

where σ, $\bar{\varepsilon}$, $\dot{\varepsilon}$ and $\dot{\varepsilon}_0$ are the flow stress, the equivalent plastic strain, the equivalent plastic strain rate and the reference strain rate, respectively. T_r is the reference temperature, T_m is the melting point of materials and T is the temperature of workpiece. A, B, n, C and m are initial yield stress of the material, the strain hardening constant, the strain hardening index, the material characteristic coefficient index and temperature sensitivity index, respectively. The first term on the right-hand side of the equation describes the strain hardening effect of the material. The second term reflects the flow stress as a function of the logarithmic strain rate, and the third term reflects the exponential decrease of the flow stress as the temperature increases. The physical properties of 45 carbon steel and cutting tool are shown in Table B.1 and the Johnson-Cook parameters used to simulate the behaviour of 45 carbon steel are specified in Table B.2 [60].

3.2. Chip separation criterion

Metal cutting is the process of material removal to form a chip, which curling and breakage affect the quality of the machined surface. The cutting chip is also a reflection of the three main factors, namely the cutting force, cutting temperature and tool wear during the cutting process. Appropriate criteria are needed to determine material and chip separation conditions to accurately simulate a chip formation process. The mechanism of chip formation involving ductile damage of materials basically occurs in two steps. The first step defines the initiation phase of the damage, while the second step defines the evolutionary phase of the damage [61]. The Johnson-Cook damage criterion is used to study the simulation process in this paper with the following damage accumulation law in Eq. (2) [62].

$$D = \sum \frac{\Delta\bar{\varepsilon}}{\bar{\varepsilon}_f}, \tag{2}$$

where $\Delta\bar{\varepsilon}$ is the equivalent plastic strain for element and $\bar{\varepsilon}_f$ is the equivalent plastic strain at failure. The corresponding elements is deleted and the chip is separated from the workpiece when D equals to 1. The equivalent plastic strain at failure is expressed as follows:

$$\bar{\varepsilon}_f = \left[d_1 + d_2\exp\left(d_3\frac{p}{q}\right)\right] \times \left[1 + d_4\ln\left(\frac{\dot{\varepsilon}}{\dot{\varepsilon}_0}\right)\right] \times \left[1 + d_5\left(\frac{T - T_r}{T_m - T_r}\right)\right], \tag{3}$$

where d_1 represents the initial failure strain; d_2 is a constant for the exponential component; d_3 accounts for the triaxiality; d_4 is the strain rate constant d_5 is the temperature factor; p is the average normal stress; and q is the Mises equivalent stress. This model incorporates the effects of stress triaxiality (p/q), strain rate and temperature on material ductility and is widely used to predict the fracture behavior of metallic materials at high strain rates. The damage constants of 45 carbon steel are listed in Table B.2. The damage evolution of a plastic material under uniaxial stress-strain response is shown in Fig. 2. Stage a-b are the linear

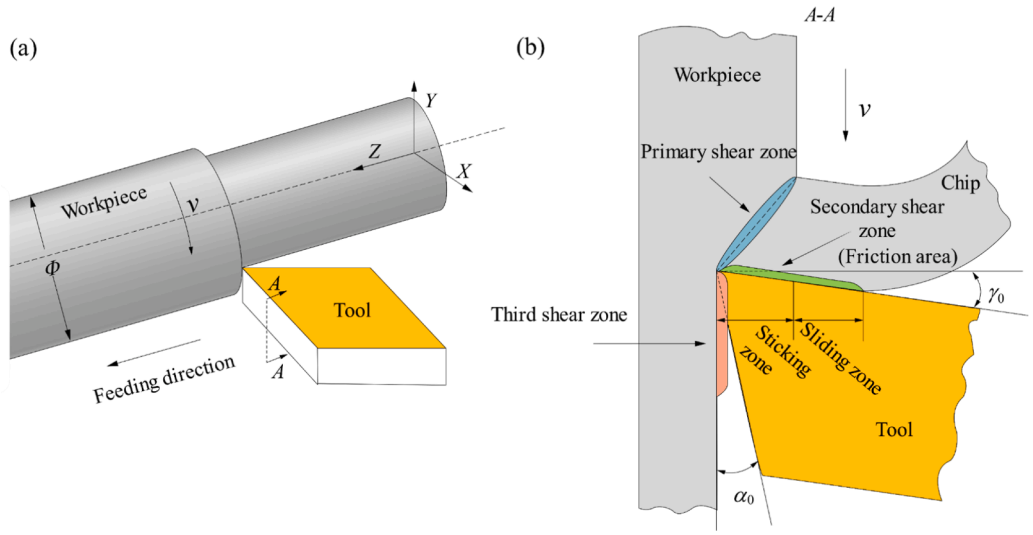

Fig. 3. Contact zones between a tool, workpiece and chip. Schematic of the (a) 3D turning process and (b) different zones of contact between the tool, workpiece and chip. The contact area between tool and workpiece can be divided into three deformation zones: primary shear zone, secondary shear zone and third deformation zone. The tool and workpiece friction are mainly concentrated in the secondary shear zone.

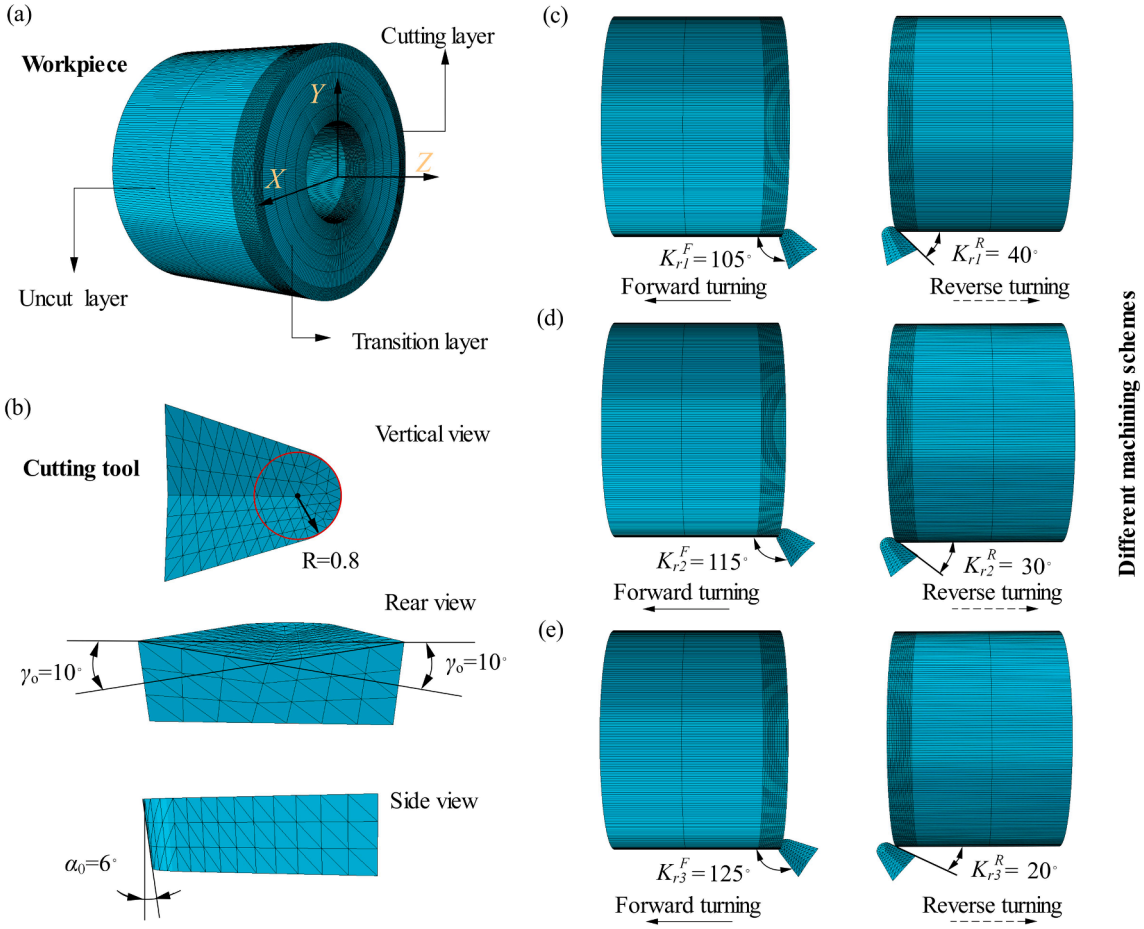

Fig. 4. MDC Finite Element models; (a) workpiece model is divided into uncut layers, transition layers, and cutting layers to improve the solution efficiency; (b) tool tip radius is 0.8 mm, rake angle γ_0 is 10°, relief angle α_0 is 6°. Cutting tool parameters; (c) tool cutting edge angle in Scheme 1 k_{r1}^{F} is 105° and reverse tool cutting edge angle k_{r1}^{R} is 40°; (d) tool cutting edge angle in Scheme 2 k_{r2}^{F} is 115° and reverse tool cutting edge angle k_{r2}^{R} is 30°; (e) tool cutting edge angle in Scheme 3 k_{r3}^{F} is 125° and reverse tool cutting edge angle k_{r3}^{R} is 20°.

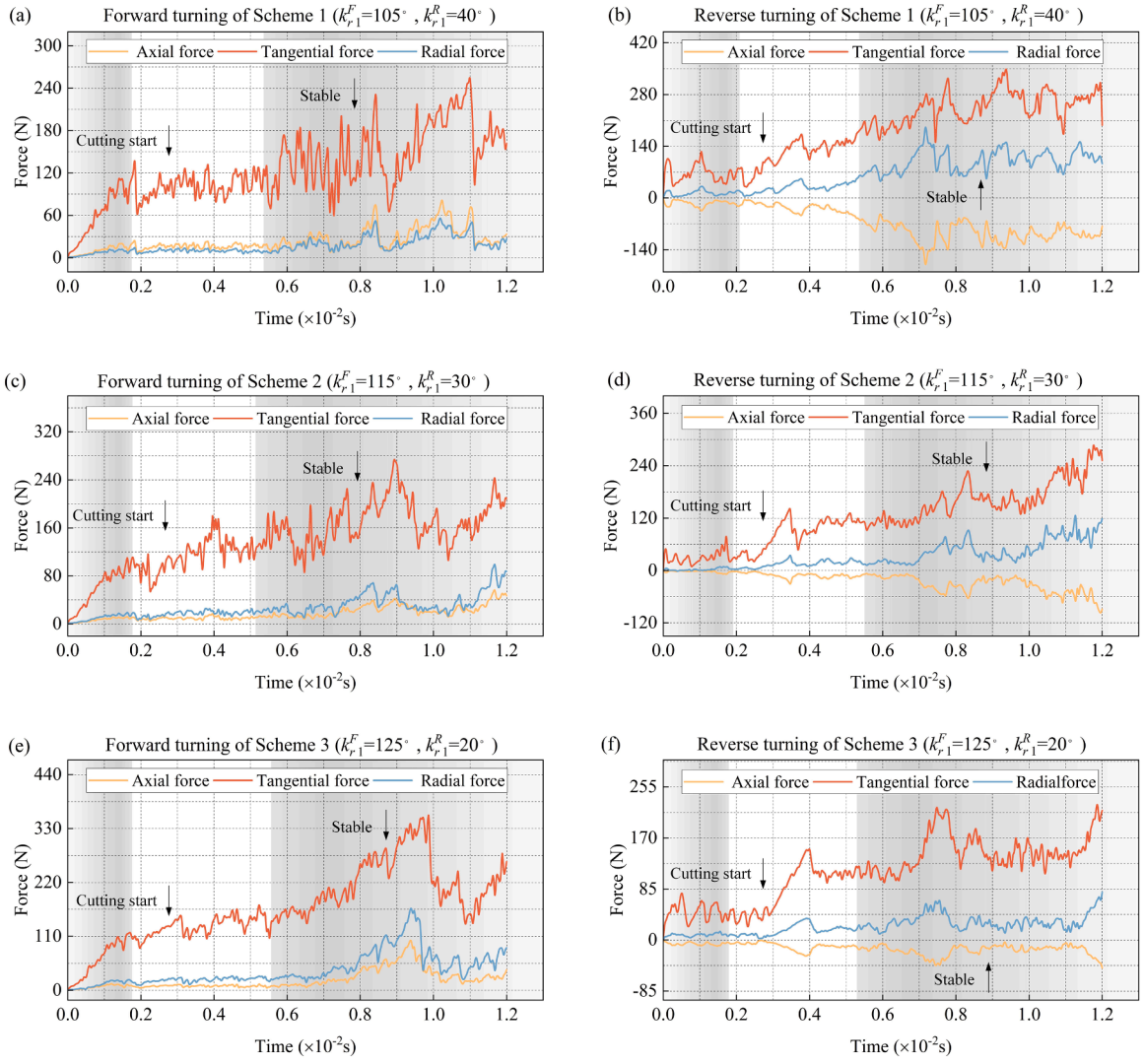

Fig. 5. Simulated time evolution of the cutting forces. Triaxial force evolutions of (a) forward turning using Scheme 1; (b) reverse turning using Scheme 1; (c) forward turning using Scheme 2; (d) reverse turning using Scheme 2; (e) forward turning using Scheme 3; (f) reverse turning using Scheme 3. The tangential force dominates in the cutting component. Forward cutting force presents stable stage faster than reverse cutting force and the cutting force of Scheme 1 is relatively small.

elastic stage, and stage b-c are the plastic yielding with strain response. When the stress increases and exceeds the yield stress, the material enters the stable plastic deformation stage c-d. The plastic instability starts when the damage parameter is equal to zero and enters the stage d-e. At point e, the stiffness of the material is completely degraded and the crack initiates as an indication of failure [63].

3.3. Friction and heat generation model

The friction between the tool and the chip plays an important role in the metal cutting process [64]. Friction originates from the interaction between the chip flow and the rake face of the tool, which affects tool wear, cutting temperature, chip formation performance. The tool and workpiece contact area can be divided into three deformation zones. Where the second deformation zone produces the largest frictional force, the friction is severe. The second deformation zone can be further divided into sliding and sticking zones [41]. As shown in Fig. 3, the area close to the tool tip is the sticking zone, and the area far from the tool tip is the sliding zone. The frictional effects of the two contact zones can be expressed by the Eq. (4) and Eq. (5), respectively.

$$\tau_f = \mu\sigma_n, if\ \mu\sigma_n < m\tau_{max}, (\text{sliding zone}), \tag{4}$$

$$\tau_f = m\tau_{max}, if\ \mu\sigma_n \geq m\tau_{max}, (\text{sticking zone}), \tag{5}$$

where τ_f is the friction force; σ_n is the normal stress; m is the shear friction coefficient; μ is the Coulomb friction coefficient; and τ_{max} is the ultimate shear flow stress which can be calculated by $\tau_{max} = \frac{\sigma_y}{\sqrt{3}}$, where $\sigma_y$is the yield strength of the material. The constant shear friction coefficient m in this study is set to be one.

Most of the energy of the cutting process is converted into heat, which makes the temperature of the cutting zone to increase. The heat is generated mainly by plastic deformation and friction at the chip interface of the tool. The heat generated by plastic deformation can be expressed by the following equation:

$$\dot{q}_p = \eta_p \bar{\sigma}\dot{\bar{\varepsilon}}, \tag{6}$$

where $\dot{q}_p$ is the heat generation rate and η_p is the inelastic heat fraction taken as 0.9 in this study [63]. The heat generated by friction can be evaluated as [65]:

$$q_f = \rho C_p \frac{\Delta T_f}{\Delta t} = \eta_f J \tau_f \gamma, \tag{7}$$

where $\tau_f$is the shear stress determined by Coulomb's friction law and γ is

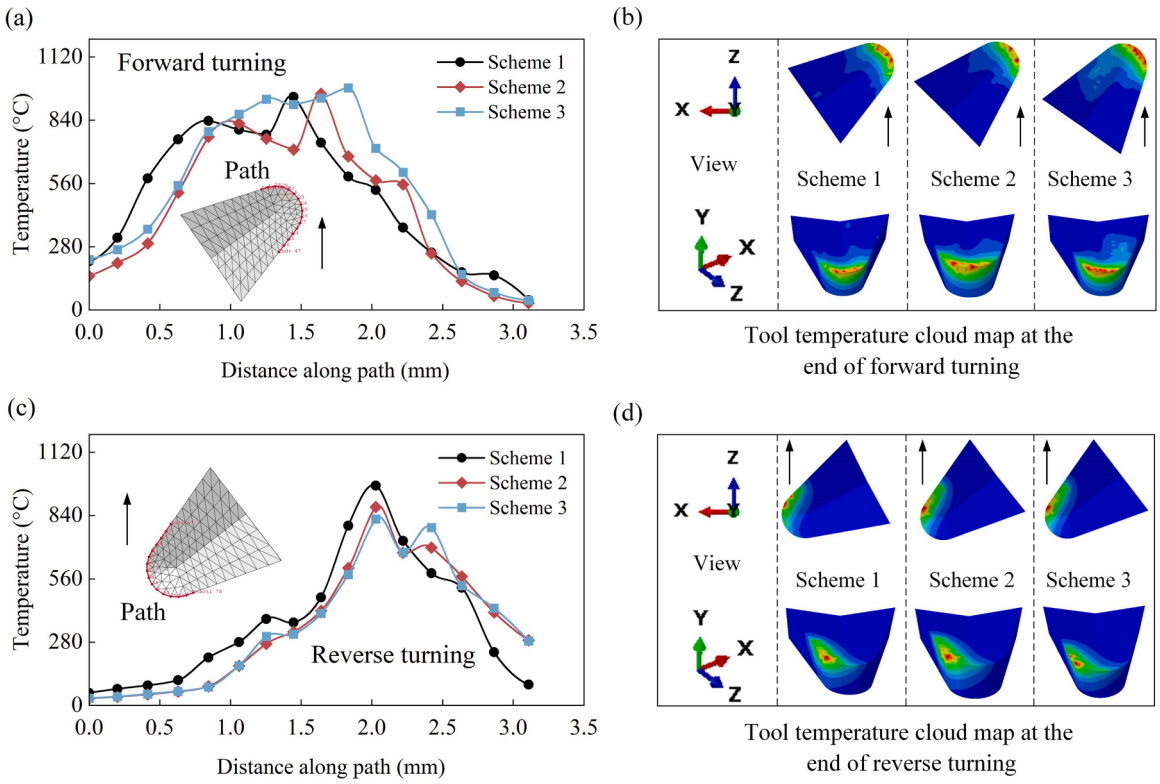

Fig. 6. Simulation of cutting temperature distribution. Comparison of (a) cutting temperature for forward turning of three machining schemes (Scheme 1, 2 and 3). Comparison of (b) tool temperature cloud map for forward turning of three machining schemes (Scheme 1, 2 and 3). Comparison of (c) tool temperature cloud map for reverse turning of three machining schemes (Scheme 1, 2 and 3). Comparison of cutting (d) temperature for forward turning of three machining schemes (Scheme 1, 2 and 3). The heat of the tool in forward turning is mainly concentrated at the tool tip. The heat of the tool in reverse turning is mainly concentrated on the cutting side of the tool tip. The cutting temperature of Scheme 3 is lower compared to the other two schemes.

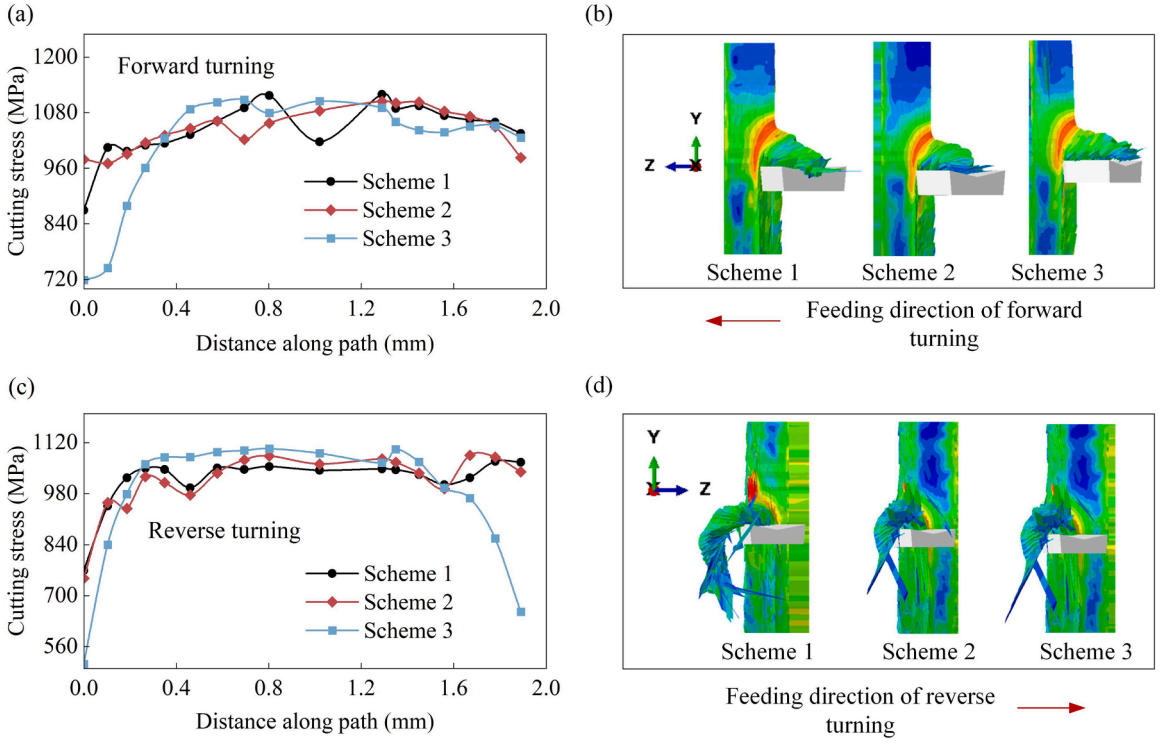

Fig. 7. Simulated cutting stress distributions. Cutting stresses for (a) forward turning and (c) reverse turning of three machining schemes (Scheme 1, 2 and 3). Comparison of (b) cutting stress cloud maps for (b) forward turning and (d) reverse turning of three machining schemes (Scheme 1, 2 and 3). Cutting stress is mainly concentrated in the primary shear zone. The cutting stress of Scheme 2 is lower compared to the other two schemes.

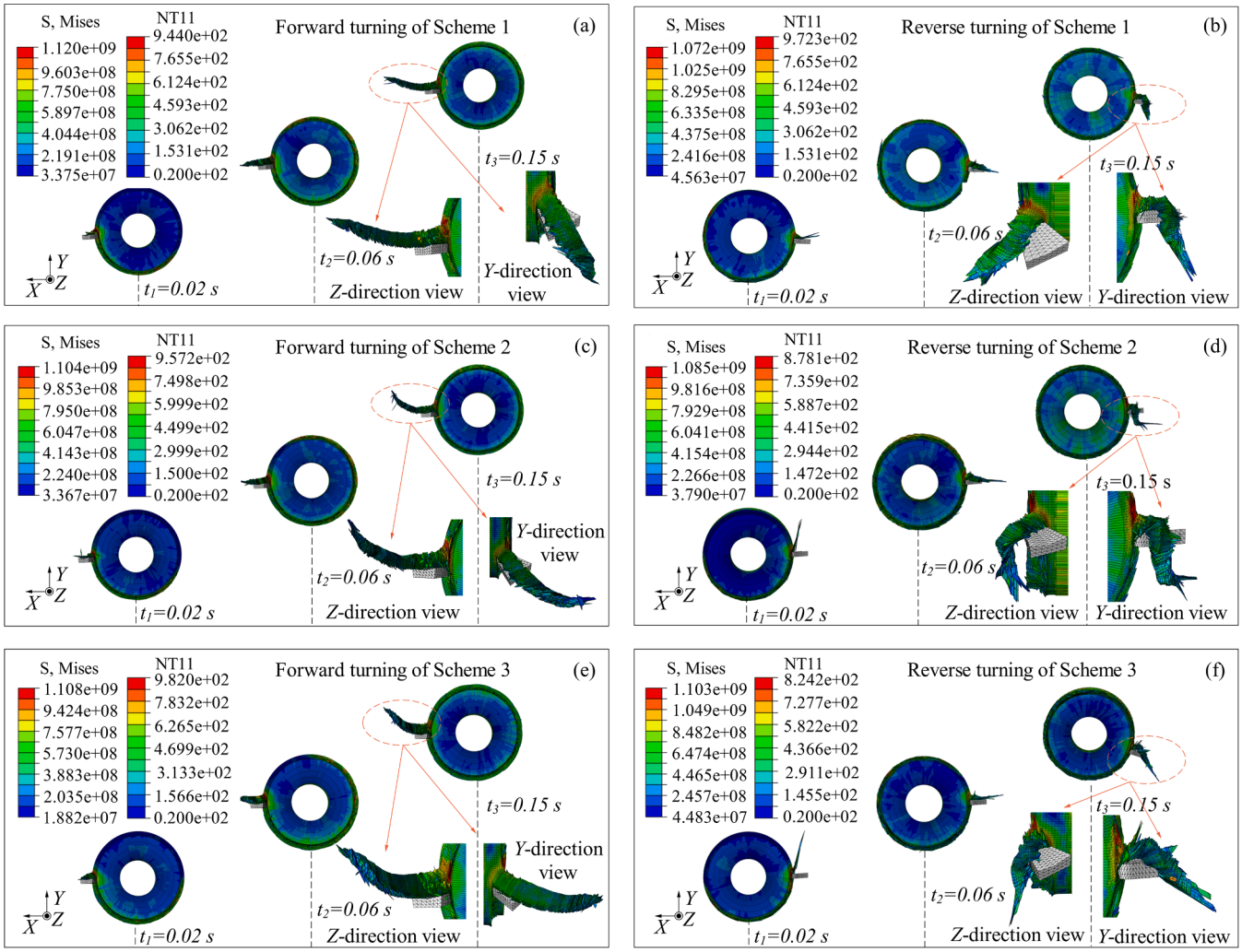

Fig. 8. Cutting process simulation showing chip formations. There are significant differences in chip formation between (a) forward and (b) reverse turning for Scheme 1, (c) forward turning and (d) reverse turning using Scheme 2, and (e) forward turning and (f) reverse turning using Scheme 3. Chip morphologies were observed from the *X*-axis and *Y*-axis directions at machining times t_1=0.02 s, t_2=0.06 s and t_3=0.15 s. S, Mises represents the cutting stress value, NT11 represents the cutting temperature value. The chip curling was most intense for Scheme 3 in forward turning, and more sever and integrity for Scheme 2 in reverse turning. By comparing the final morphology of chips, Scheme 2 chip breakage is more conducive to smooth MDT machining.

the slip strain rate. η_f is the dissipated energy, of which the amount of *J* is carried away by the chip and the rest (1-*J*) by the tool.

3.4. Finite element simulation model

The tool and the cylindrical bar are constructed, and three machining schemes are established with tool cutting edge angle as variables. Each assembly model is shown in Fig. 4(c), (d) and (e), respectively. The tool tip radius is 35°. The tool cutting edge angle in Scheme 1 is 105°, and end cutting edge angle is 40°. The tool cutting edge angle in Scheme 2 is 115° and end cutting edge angle is 30°. The tool cutting edge angle in Scheme 3 is 125°, and end cutting edge angle is 20°. The tool adopts a symmetrical structure and the main parameters are shown in Fig. 4(b), similar as modelled in [66,67]. The tool material is carbide and the physical properties are shown in Table B.1. The workpiece and tool are assumed to be elastic and isotropic, irrespective of the changes in the internal metallographic organization and chemistry of the material. To save the simulation calculation time, the workpiece is set as a hollow cylindrical bar [39]. As shown in Fig. 4(a), the workpiece is divided into cutting layer, transition layer, and uncut layer, and the grid is encrypted for the cutting layer. The workpiece is meshed using C3D8t elements and contains 149,464 nodes and 135,648 elements. The tool is divided with a tetrahedral mesh (C3D10MT), containing 6701 nodes and 4160 meshes. Furthermore, the tool is assumed to be a rigid body as the tool hardness is much higher than the workpiece. The contact between the tool and the workpiece is defined as surface-to-surface contact, with the main face as the tool face and the material as the slave face. The mechanical constraint formulation is selected as penalty contact method with a friction coefficient of 0.4. Setting the initial environment temperature to 20 °C and the boundary layer heat dissipation coefficient to 20 W/m^2. The analysis step is selected as Dynamic, Temp-disp, Explicit, with a target time increment of 1e-08. The workpiece is coupled to the reference point at the origin, giving the reference point a rotational velocity around the *Z*-axis, with the other directions of motion fixed. The tool is coupled to a reference point on the tool, giving the reference point a feeding speed (positive for forward turning and negative for reverse turning) along the *Z*-axis, with the other directions of motion fixed. The cutting speed is 144.44 m/min, feeding speed is 0.15 mm/rev and the depth of cut is 0.4 mm. The solution time of the analysis step module, i.e., the turning time, is set to 0.15 s. The solution time for each simulation was approximately 20 h on a computer with an 11th generation Intel(R) Core(TM) i7-11800H @ 2.30 GHz processor.

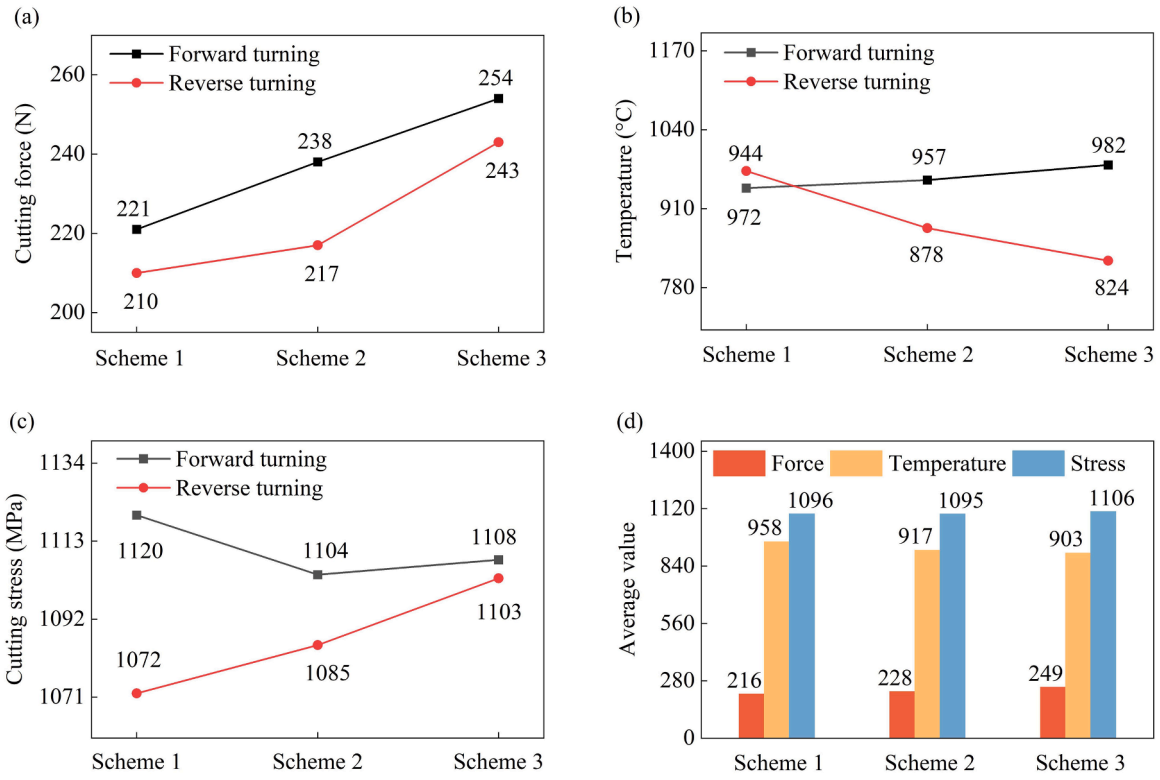

Fig. 9. Comparison of simulated forces, stresses and temperatures. Comparison of the (a) cutting forces, (b) temperatures and (c) stresses average values for the three machining schemes. Take the (d) average of the results for forward turning and reverse turning to compare. Scheme 1 has lower cutting force, but higher cutting temperature, and Scheme 3 has lower cutting temperature, but higher cutting force. It is concluded that Scheme 2 has balanced performance in terms of cutting force, cutting temperature, cutting stress and chip, which is more favorable for MDT machining.

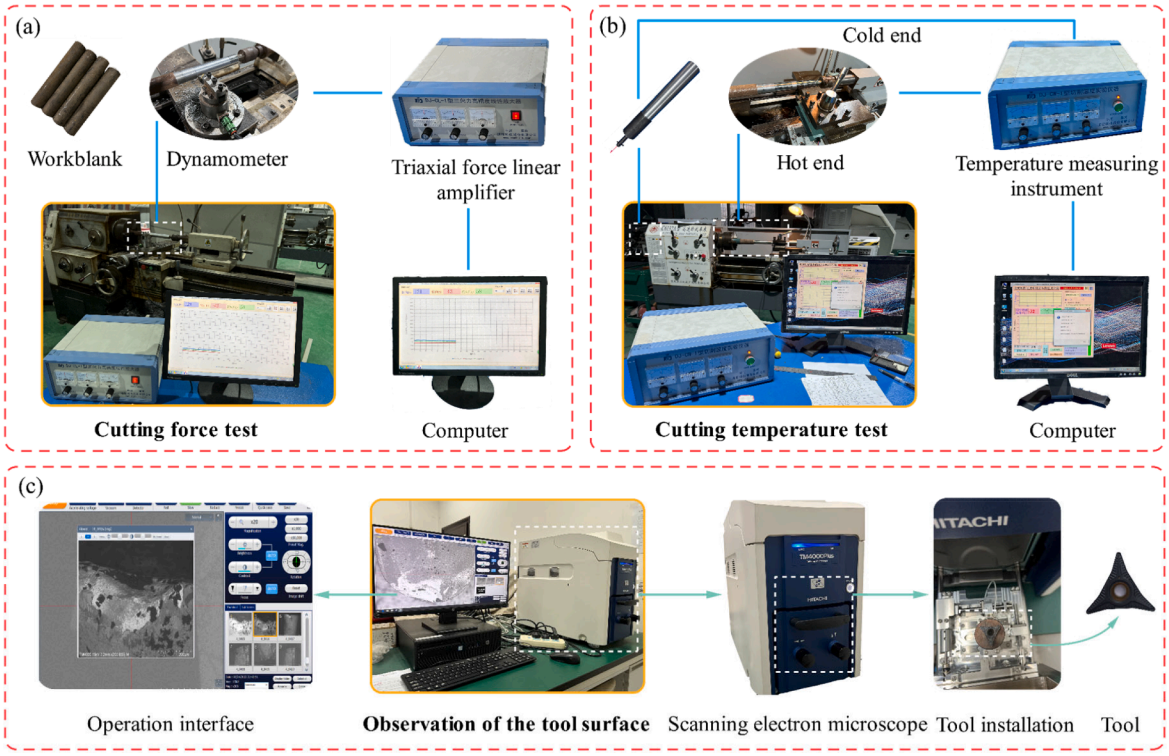

Fig. 10. Experimental set ups and instrumentation used to measure: (a) cutting forces, (b) cutting temperatures and (c) microscopic surfaces of tool. The cutting force test and cutting temperature test are conducted on CA6140A and C6132A lathes, respectively. 45 carbon steel is used for orthogonal experimental machining. Cutting force and temperature are obtained by DJ-CL-1 triaxial forces high-precision linear amplifier and DJ-CW-1 cutting temperature experimental instrument, respectively.

Table 1
Three-factor, four-level orthogonal experimental parameters for studying MDT cutting forces and temperatures.

Level	Variable Cutting speed, v (m/min)	Feeding speed, f (mm/rev)	Depth of cut, a_p (mm)
1	94.95	0.10	0.10
2	120.58	0.15	0.20
3	144.44	0.20	0.30
4	173.33	0.24	0.40

3.5. Simulation results and analysis

The variation values of cutting force during the simulation machining are shown in Fig. 5(a)–(f). In the turning process, the cutting force fluctuates greatly with time caused by the destruction of the grid cell. In Scheme 1, the tangential force is the maximum among the cutting forces, followed by the axial force and the radial force is the minimum. In Schemes 2 and 3, the tangential force is the maximum among the cutting forces, followed by the radial force and the axial force is the minimum. The direction of axial force during reverse turning is opposite

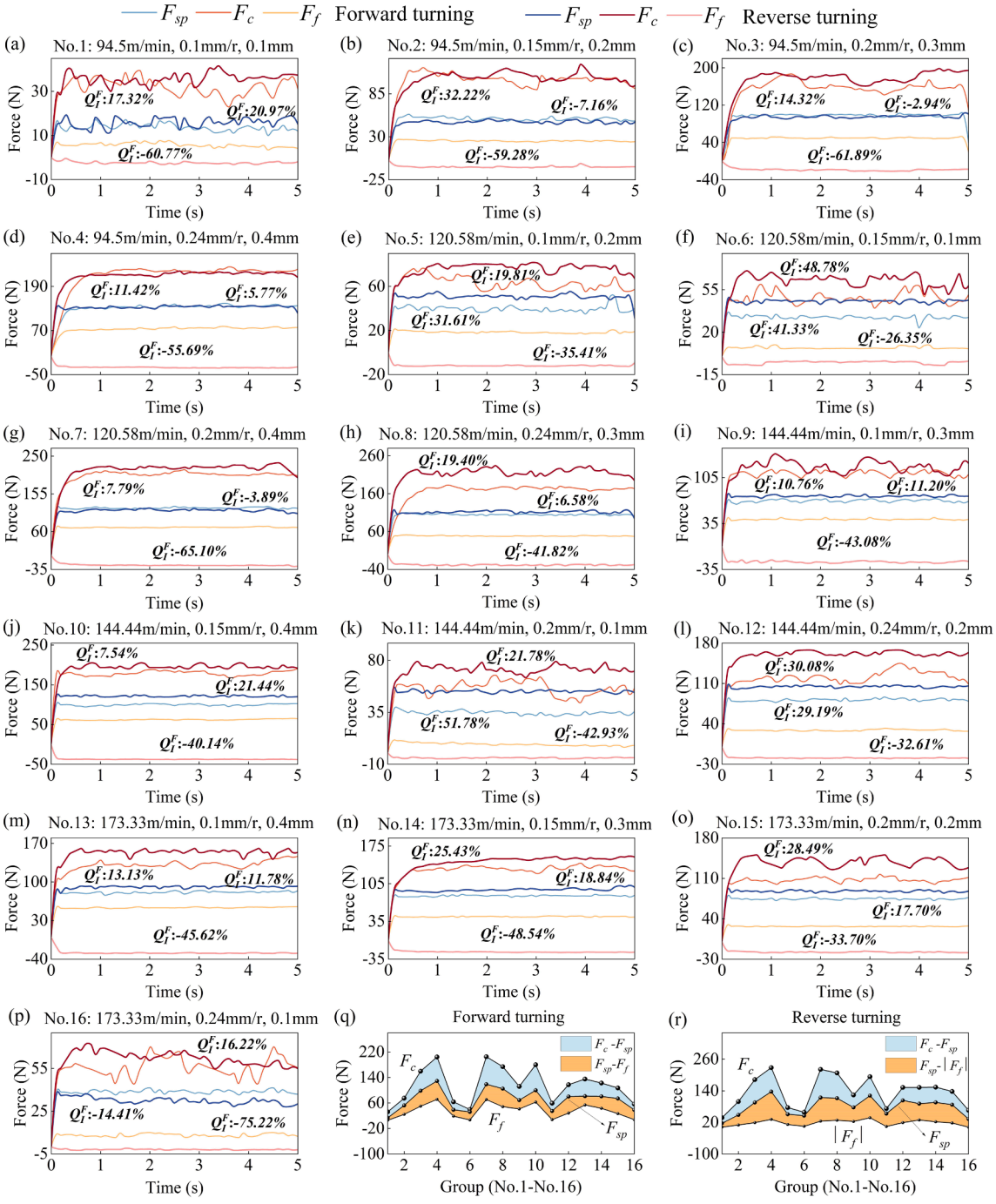

Fig. 11. Experimental triaxial forces for forward and reverse turning for different cutting parameters. The effect of cutting speed are shown in (a)–(d) first level, (e)–(h) second level, (i)–(l) third level and (m)–(p) fourth level. Factor Q_I^F is calculated as $(F_{Reverse}\text{-}F_{Forward})/F_{Forward}$. The tangential and radial forces of reverse turning are generally higher than those of forward turning, and the axial forces of reverse turning are smaller than those of forward turning and in the opposite direction. The tangential force is significantly greater than the radial and axial forces in the triaxial force of (q) forward turning and (r) reverse turning for each group.

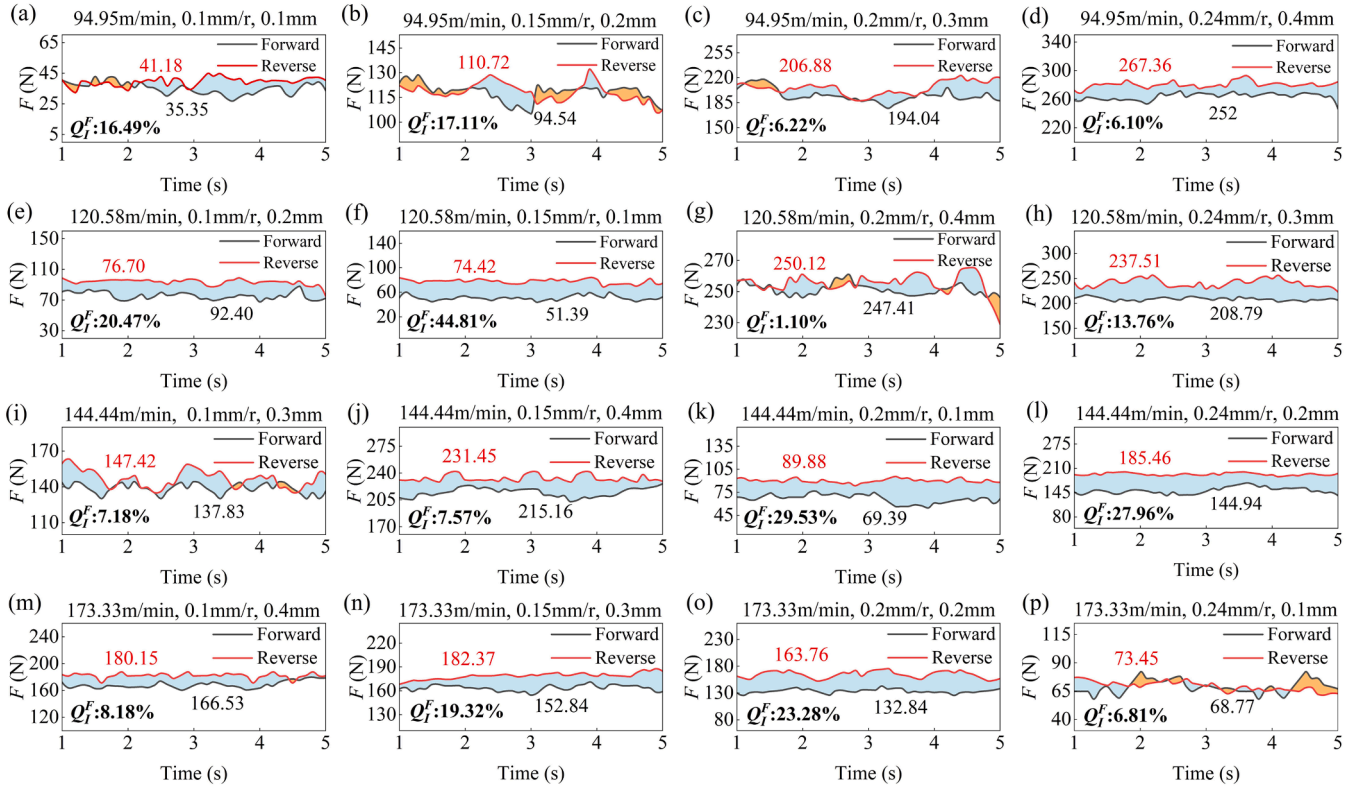

Fig. 12. Experimental time evolution of the main cutting forces for forward and reverse turning for different cutting parameters. The effect of cutting speed is shown in (a)–(d) first level, (e)–(h) second level, (i)–(l) third level and (m)–(p) fourth level. The cutting parameters in the figure are cutting speed, feeding speed and depth of cut in that order. The main cutting force of reverse turning is generally higher than that of forward turning. The blue area indicates that the reverse cutting force is higher than the forward cutting force, and the yellow area indicates that the reverse cutting force is lower than the forward cutting force.

to that of forward turning. In forward turning, when the tool cutting edge angle is 105°, the main cutting force, tangential force and radial force are minimized. The tangential force and radial force are maximum when the tool cutting edge angle is 125°. The axial force is maximum when the tool cutting edge angle is 105°. The result shows that the main cutting force, tangential force and radial force tends to increase when the tool cutting edge angle is between 105° and 125°. The axial force tends to decrease when the tool cutting edge angle is between 105° and 125°. In reverse turning, the main cutting force, radial force and tangential force are minimum when the reverse tool cutting edge angle is 40°. The tangential force and radial force are maximum when the reverse tool cutting edge angle is 20°. The axial force is maximum when the reverse tool cutting edge angle is 40°. The above shows that the main cutting force and radial force tends to decrease when the reverse tool cutting edge angle is between 20° and 40°. The axial force tends to increase when the tool cutting edge angle is between 20° and 40°. The average values of the main cutting forces for the three schemes are shown in Fig. 9(a). The average cutting force in Scheme 1 is the minimum, followed by Scheme 2, and the cutting force in Scheme 3 is the maximum. Therefore, when the tool cutting edge angle is 105° and end cutting edge angle is 40°, the cutting force is in a smaller range.

The cutting-edge temperatures of the tools for forward and reverse turning for three different machining schemes are shown in Fig. 6(a) and (c), whereas the surface temperature cloud maps of the tool are depicted in Fig. 6(b) and (d). In the forward turning, the high temperatures are located at the tip of the tool, and the heat diffusion outward shows an increasing trend when the tool cutting edge angle is between 105° and 125°. In the reverse turning, the high temperatures are on the cutting side of the tool tip, and the heat distribution area shows an increasing trend when the tool cutting edge angle is between 20° and 40°. The maximum cutting temperatures for three different machining schemes are shown in Fig. 9(b). In the forward turning, the cutting temperature is minimum when the tool cutting edge angle is 105° and maximum when the tool cutting edge angle is 125°. When the tool cutting edge angle is 125°, the cutting temperature is 982 ℃, and when the tool cutting edge angle is 105°, the cutting temperature is 944 ℃, with a difference of 4.03%. In reverse turning, the cutting temperature is maximum when the reverse tool cutting edge angle is 40° and minimum when the reverse tool cutting edge angle is 20°. When the reverse tool cutting edge angle is 40°, the cutting temperature is 972 ℃. When the reverse tool cutting edge angle is 20°, the cutting temperature is 824 ℃, with a difference of 15.22%. The average cutting temperature is shown in Fig. 9(d). Scheme 3 has the lowest average cutting temperature and Scheme 1 has the highest average cutting temperature. The lowest average cutting temperature are obtained in Scheme 3.

The cutting stresses in the primary shear zone for each scheme are shown in Fig. 7(a) and (c). The stress cloud maps of primary shear zone are shown in Fig. 7(b) and (d). The stress is mainly concentrated in the primary shear zone. The maximum cutting stresses for three different machining schemes are shown in Fig. 9(c). In the forward turning, when the tool cutting edge angle is 105°, the stress in the cutting zone is maximum. When the tool cutting edge angle is 115°, the stress in the cutting zone is minimum. In the reverse turning, when the reverse tool cutting edge angle is 20°, the stress in the cutting zone is maximum. When the reverse tool cutting edge angle is 40°, the stress in the cutting zone is minimum. The average cutting stress is shown in Fig. 9(d). It can be deduced that the average stress of Scheme 3 is the largest, followed by Scheme 1, and the average stress of Scheme 2 is the smallest.

The chip formation process for each cutting scheme is shown in Fig. 8. In forward turning, the radius of chip curl decreases as the tool cutting edge angle increases. The chip curling is most severe when the tool cutting edge angle is 125°. The more severe the chip curl, the more

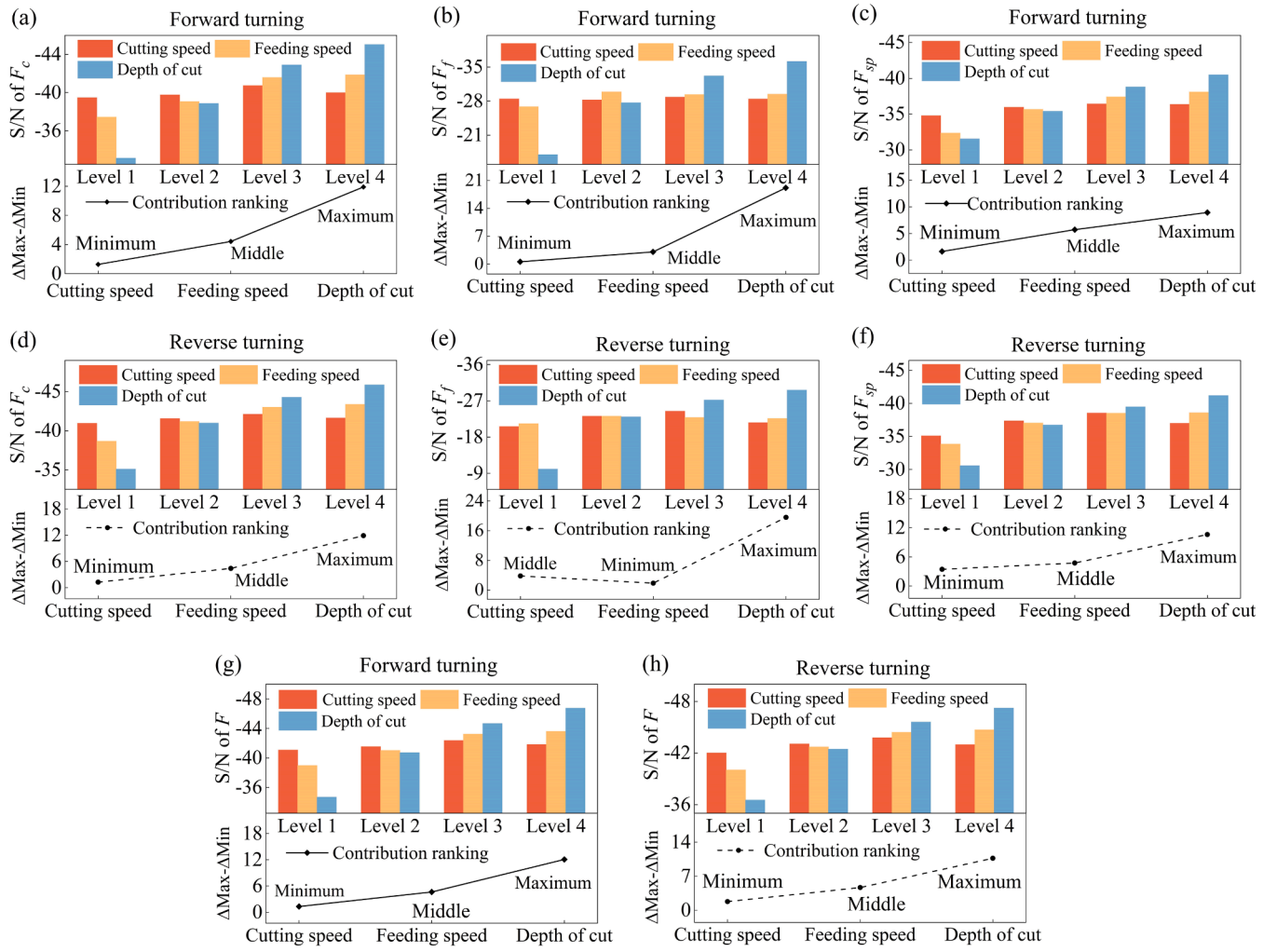

Fig. 13. Overview of cutting parameters influence on the cutting force. S/N ratio and cutting parameters contribution ranking of (a) forward turning tangential force, (b) axial force, (c) radial force and (g) main cutting force, which are maximally affected by depth of cut, followed by feeding speed and minimum cutting speed. S/N ratio and cutting parameters contribution ranking of (d) reverse turning tangential force, (e) axial force, (f) radial force and (h) main cutting force, which axial forces are maximally affected by depth of cut, followed by cutting speed and minimum feeding speed, and the contribution ranking of other forces is the same as that of forward turning.

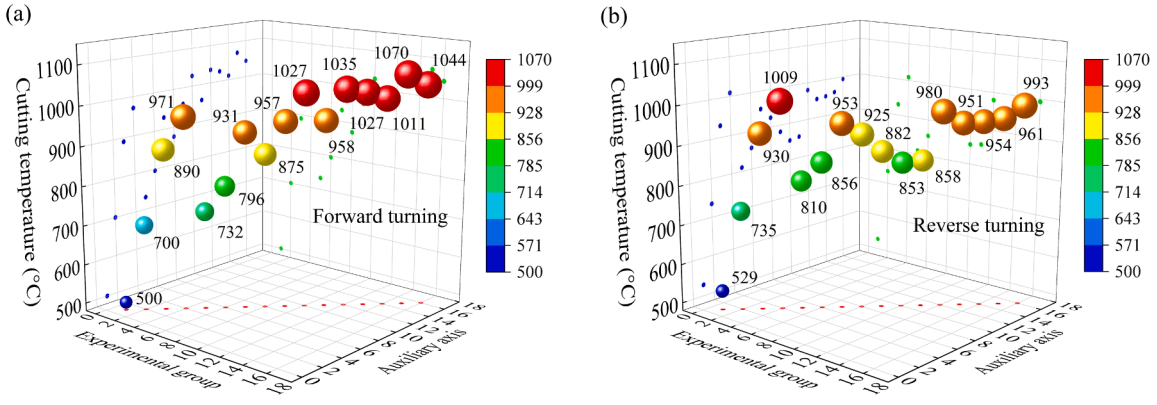

Fig. 14. Experimental temperatures for different cutting parameters. There is a significant difference in temperature for (a) forward turning and (b) reverse turning. Cutting temperature values are expressed by label symbols and colors. In groups 1 to 8, the cutting temperature for forward turning is lower than that for reverse turning, and in groups 9 to 16, the cutting temperature for forward turning is higher than that for reverse turning.

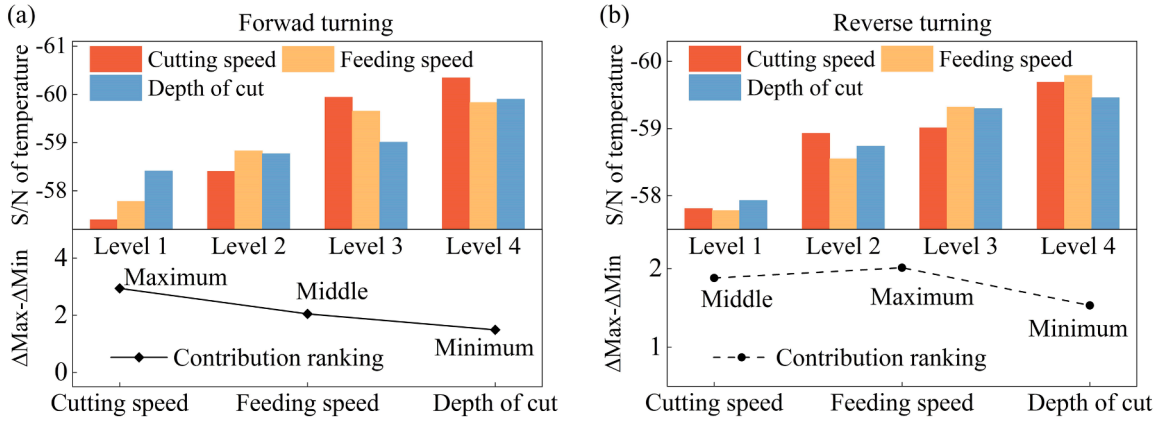

Fig. 15. The main response of the cutting temperature. The S/N of (a) forward cutting temperature and (b) reverse cutting temperature. The cutting temperature of forward turning is maximally affected by the cutting speed, while the cutting temperature of reverse cutting is maximally affected by the feeding speed.

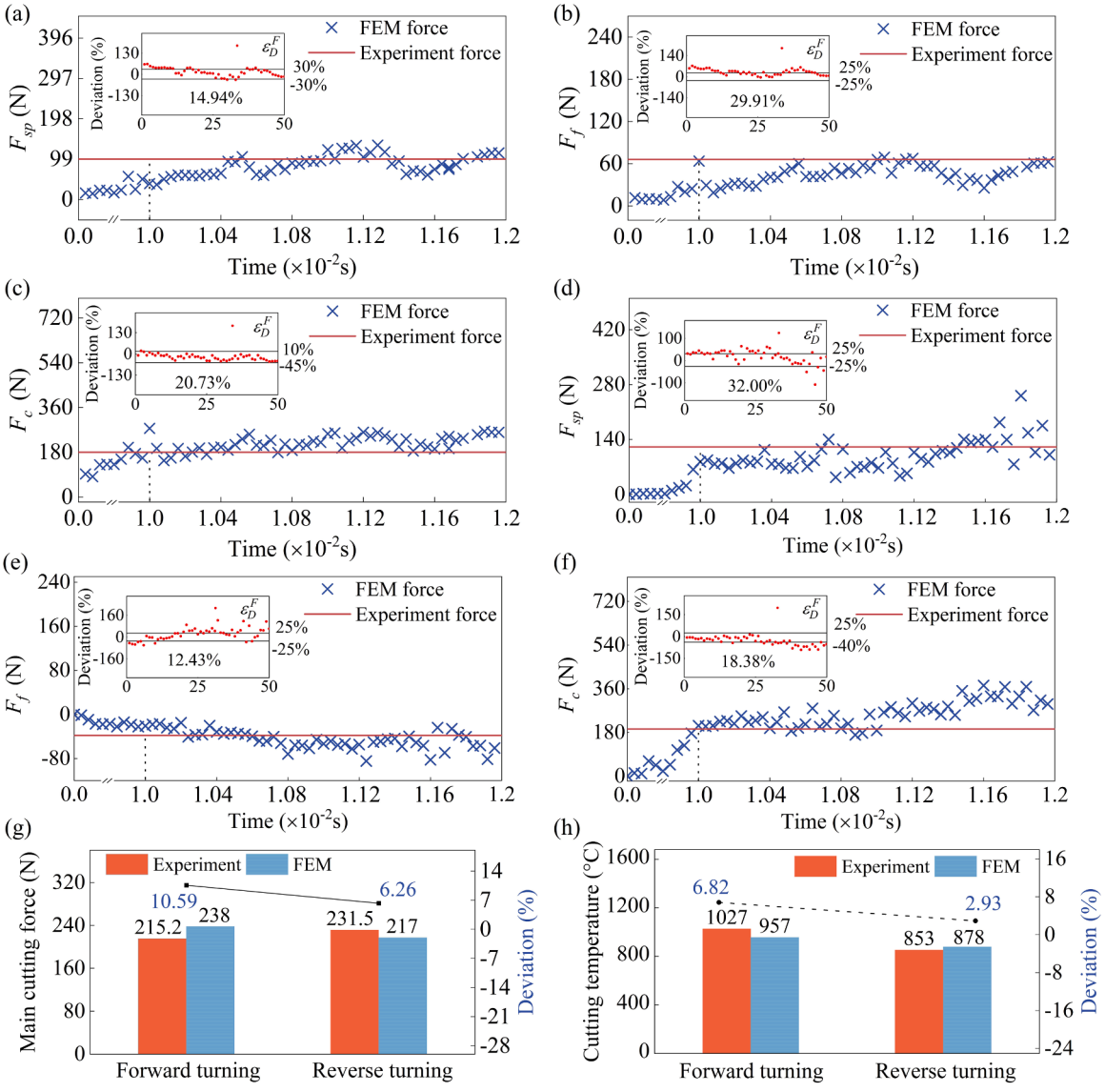

Fig. 16. Comparisons of cutting force and cutting temperature obtained from simulation and experiments for $v = 144.44$ m/min, $f = 0.15$ mm/rev, a_p=0.4 mm. The deviations of radial force, axial force and tangential force for forward cutting are (a) 14.94%, (b) 29.91% and (c) 20.73%, respectively. The deviations of radial force, axial force and tangential force for reverse turning are (d) 32.00%, (e) 12.43% and (f) 18.38%, respectively. The (g) main cutting force deviation for forward turning is 10.59% while the reverse cutting is 6.26%, and the (h) temperature deviation for forward turning is 6.82% while the reverse turning is 2.93%.

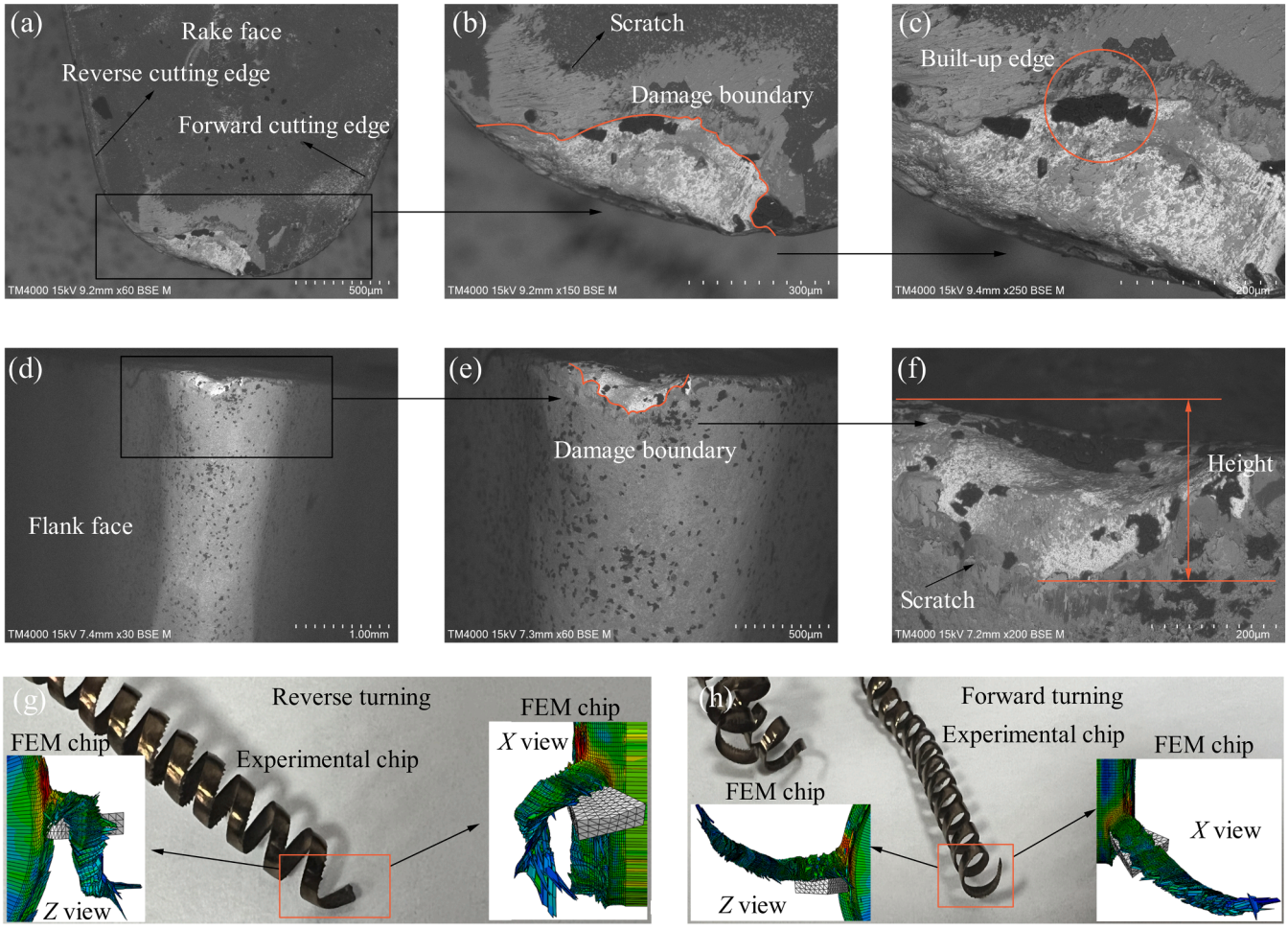

Fig. 17. Microscopic surface analysis and a comparison of the chip morphology obtained from the simulation and experiments. (a) Crescent-shaped damage appears in rake face near the reverse cutting edge and formation of (c) built-up edge. Scratches appear on both (b) rake and (f) flank faces of the tool. Simulated and experimental chip morphologies of (g) forward turning and (h) reverse turning match in X and Z views.

Table B.1
Physical properties of 45 carbon steel and cutting tool.

Property	Workpiece (45 carbon steel)	Tool (Cemented carbide)
Density ρ (kg·m^{-3})	7890	14,850
Inelastic heat fraction	0.90	–
T_m (℃)	1460	–
T_r (℃)	20	20
Conductivity k (W·m^{-1}·K^{-1})	(48.15, 100); (46.47, 200); (43.96, 300); (41.45, 400); (38.01, 500); (35.17, 600); (31.82, 700); (25.96, 800);	75
Specific heat c (J·kg^{-1}·K^{-1})	(480, 100); (498, 200); (524, 300); (560, 400); (615, 5 00); (700, 600); (854, 700); (1064, 800); (806, 900)	176
Young's modulus E (GPa, ℃)	(209, 20); (207, 100); (202, 200); (196, 300); (186, 400); (174, 500)	640
Poisson's ratio ν (℃)	(0.269, 20); (0.270, 100); (0.290, 200); (0.312, 300); (0.309, 400); (0.308, 500)	0.25
Thermal expansion α (×10^{-6} ℃$^{-1}$, ℃)	(11.59, 20); (12.32, 100); (13.09, 200); (13.71, 300); (14.18, 400); (14.67, 500)	–

conducive to chip breakage [68]. The chip is broken smoothly, which facilitates to overcome the tendency of chip tangling during MDT machining [69]. In reverse turning, chip curl is generally more severe than that of forward turning. When the reverse tool cutting edge angle is 30°, the chip curl degree is higher and more integrity. In a comprehensive analysis, when the tool cutting edge angle is 115°, it is beneficial for the chip control. Smaller cutting temperature and force are beneficial for extending tool life and reducing machine energy consumption, while stable chip breakage is beneficial for workpiece surface integrity. Therefore, Scheme 2 is more suitable for the MDT performance improvement and further study.

4. Investigation and verification of MDC properties

In practical operation, the cutting performance is influenced by the cutting parameters (mainly includes cutting speed, depth of cut, feeding speed) [58]. Choosing the suitable cutting parameters is essential to improve processing efficiency and reduce tool wear [70]. In this section, the optimal machining scheme for experiments is obtained from simulation. Effects of cutting parameters on its cutting features is analyzed by Taguchi method.

4.1. Object of analysis

According to the above simulation results, Scheme 2, where the tool cutting edge angle is 115° and end cutting edge angle is 30°, is chosen for experimental validation and further study. The cutting force and temperature are recorded during the experiment, and some chips are collected to compare with the simulation results. The cutting force test and cutting temperature test are conducted on CA6140A and C6132A

Table B.2
Johnson-Cook material parameters of 45 carbon steel.

A (MPa)	B (MPa)	C	n	m	$\dot{\varepsilon}_0(s^{-1})$	d_1	d_2	d_3	d_4	d_5
553	600	0.0134	0.234	1.0	1	0.05	4.42	−2.73	0.0018	0.55

lathes, respectively. Cutting force and temperature were obtained by DJ-CL-1 triaxial forces high-precision linear amplifier and DJ-CW-1 cutting temperature experimental instrument, respectively. The cutting force test setup and environment is shown in Fig. 10(a). The used temperature sensor adopts the natural thermocouple method to determine the temperature of the cutting zone through the thermoelectric potential. The contact zone between the workpiece and the tool is the hot end, and the tail end of the tool and the workpiece lead end form the cold end. The experiments are carried out as dry cutting without the effect of cutting fluid. The cutting temperature test setup and environment is shown in Fig. 10(b). The lathe center is used to support the end of the workpiece during machining process to reduce chatter. The dimensions of 45 carbon steel sample are 500 mm in length and 50 mm in diameter. In the preparation step, the workpiece is machined to a uniform diameter of ϕ48 mm. The tool parameters are consistent with tool used for simulation and the material is carbide. The cutting force and temperature can be obtained under the same cutting parameters. Tool surface morphology is observed by scanning electron microscope after completion of the experiment.

The cutting force and temperature of forward turning and reverse turning are compared by $L_{16}(4^3)$ orthogonal experiments [69]. The results are also selected to be compared with the simulation results for verification. The orthogonal experiment is effective in reducing the number of tests and saving time, and the experimental parameters are listed in Table 1.

The smaller-the-better characteristic proposed by Taguchi method is used to study the effect of cutting parameters on the cutting performance of MDC [71]. The corresponding signal-to-noise ratio (S/N) is defined by the following equation:

$$\frac{S}{N} = -10\log\frac{1}{n}\left(\sum_{i=1}^{n} y_i^2\right), \tag{8}$$

where n is the total number of measurements; and y_i is the ith measurement data. The relationship between the triaxial forces and the main cutting force is defined by following equation:

$$F = 2\sqrt{F_c^2 + F_f^2 + F_{sp}^2}, \tag{9}$$

where F is the main cutting force; and F_c is the tangential force; F_f and F_{sp} are the axial force and radial force, respectively.

4.2. Results and discussions

The triaxial forces obtained from the orthogonal experiment and main cutting forces for forward turning and reverse turning are shown in Table B.3. Obviously, the tangential and radial forces in reverse turning are generally higher than those in forward turning. The main cutting force of reverse turning is also higher than that of forward turning. The direction of axial force of reverse turning is opposite to that of forward turning, meanwhile, the axial force of reverse turning is lower than that of forward turning. Difference between radial and axial components is attributed to the variation of the effective tool cutting edge angle. The decrease of reverse tool cutting edge angle resulting in an increase in the radial component force and a reduction in the axial component force. In reverse turning, the cutting edge involved in material removal is larger, and the material removal per unit time increases, causing an increase in the main cutting force. The tangential force is the maximum among the triaxial forces, followed by the radial force, and the axial force is the minimum. Both in forward and reverse turning, the radial force is about half of the tangential force.

The comparison of the triaxial forces variation between forward turning and reverse turning with different cutting parameters is shown in Fig. 11. The tangential force of reverse turning is about 20% higher than that of forward turning, and the maximum ratio is 48.78%, minimum is 7.54%. The radial force for reverse turning is approximately 15% higher than that for forward turning, and the maximum ratio is 51.87%, minimum is −14.41%. Under some machining conditions, the radial force of forward turning is higher than that of reverse turning. This may be related to the chatter generated during machining, which causes the separation of the tool from the workpiece for short durations. Furthermore, the axial force for forward turning is approximately 1.5 times that for the reverse turning.

The comparison of the main cutting force for the forward turning and the reverse turning is shown in Fig. 12. Under the same cutting parameters, the main cutting force of reverse cutting is generally higher than that of forward cutting. When cutting starts, the cutting force rises rapidly and then drops to a stable level for fluctuation. The main cutting force of reverse turning is about 15% higher than that of forward turning, and the maximum ratio is 44.81%, minimum is 1.10%. The main cutting force of reverse turning increases mainly because the tool cutting edge increases, the material removal rate and the resistance to overcome material deformation increases.

The signal-to-noise ratio (S/N) of the cutting force is shown in Table B.3. The main response of the cutting force S/N is plotted as shown in Fig. 13 to analyze the effect of cutting parameters visually on each cutting force. In turning operations, the tangential force is the dominant factor in determining the machine load power. Workpiece deformations and occurrences of chatter are influenced by the radial forces, which affects the roughness of the workpiece machined surface, while the axial forces have much smaller influence.

Analysis of Fig. 13 shows that each cutting parameter contributes differently to the S/N of the cutting force. The forward cutting force is maximally influenced by the depth of cut, and as the depth of cut increases, S/N starts to decrease and the cutting force starts to rise. This is attributed to the increased cutting width and back cutting depth with the increase in depth of cut, which results in an increase in the resistance of the workpiece material to cutting by the tool. The influence of feeding speed on cutting force is second only to depth of cut, with the increase of feeding speed, cutting force also rises. The cutting width per unit time is doubled when the feeding speed is twice as fast, and thus the tangential force is also doubled [72,73]. However, during the cutting process, the tool tip accumulates built up edges, which makes the actual tool rake angle of the tool increase and the tangential force decrease [74]. The cutting speed has minimal effect on the cutting force, but with the increase of cutting speed, the cutting force has the tendency to increase and then decline. The cutting force has its maximum value when the cutting speed is between 120.58 m/min and 173.33 m/min. When the cutting speed reaches a certain range, the cutting temperature grows with the increase of cutting speed, causing the reduction of friction coefficient between tool and chip, which leads to the reduction of cutting force. In the reverse cutting force, the cutting parameters have the same effect on the cutting force as in the forward turning, except for the axial force. The reverse turning axial force is maximally influenced by the depth of cut, follow by the cutting speed, and is least affected by the feeding speed. This may be attributed to the fact that the axial force for reverse turning is very low and the change is not significant when increasing the feed.

The cutting temperature obtained from the orthogonal experiment of forward turning and reverse turning are shown in Table B.3 and Fig. 14.

Table B.3
Cutting force and cutting temperature results of forward and reverse turning with different cutting parameters. Signal-to-noise ratio (S/N) is calculated by substituting the cutting force and cutting temperature values into Eq. (8). The smaller the (S/N) means the corresponding cutting temperature or cutting force is higher.

No.	1	2	3	4	5	6	7	8	9	10	11	12	13	14	15	16		
Cutting parameters	v (m/min)	94.95	94.95	94.95	94.95	120.58	120.58	120.58	120.58	144.44	144.44	144.44	144.44	173.33	173.33	173.33	173.33	
	f (mm/rev)	0.10	0.15	0.20	0.24	0.10	0.15	0.20	0.24	0.10	0.15	0.20	0.24	0.10	0.15	0.20	0.24	
	a_p (mm)	0.10	0.20	0.30	0.40	0.20	0.10	0.40	0.30	0.30	0.40	0.10	0.20	0.40	0.30	0.20	0.10	
Tangential force, F_c (N)	Forward	32.10	74.87	159.67	204.31	63.50	39.44	205.14	173.90	111.96	179.88	59.37	117.43	134.98	122.43	106.94	56.48	
	S/N	−30.13	−37.49	−44.07	−46.21	−36.06	−31.92	−46.24	−44.81	−40.98	−45.10	−35.47	−41.40	−42.61	−41.76	−40.58	−35.04	
	Reverse	37.66	98.99	182.53	227.64	76.08	58.68	221.13	207.63	124.01	193.44	72.30	152.75	152.70	153.57	137.41	65.64	
	S/N	−31.52	−39.91	−45.23	−47.14	−37.63	−35.37	−46.89	−46.35	−41.87	−45.73	−37.18	−43.68	−43.68	−43.73	−42.76	−36.34	
Axial force, F_f (N)	Forward	5.71	24.31	49.73	71.27	18.58	7.06	70.72	48.37	41.18	62.80	7.92	28.46	53.71	43.28	26.59	7.87	
	S/N	−15.13	−27.72	−33.93	−37.06	−25.38	−16.98	−36.99	−33.69	−32.29	−35.96	−17.97	−29.08	−34.60	−32.73	−28.49	−17.92	
	Reverse	−2.24	−9.90	−18.95	−31.58	−12.00	−5.20	−24.68	−28.14	−23.44	−37.59	−4.52	−19.18	−29.21	−22.27	−17.63	−1.95	
	S/N	−7.00	−19.91	−25.55	−29.99	−21.58	−14.32	−27.85	−28.99	−27.40	−31.50	−13.10	−25.66	−29.31	−26.95	−24.93	−5.80	
Radial force, F_{ap} (N)	Forward	13. 64	52.35	98.41	129.16	38.79	32.18	118.86	104.94	69.03	99.97	35.03	80.05	81.42	80.61	74.19	38.44	
	S/N	−22.70	−34.38	−39.86	−42.22	−31.77	−30.15	−41.50	−40.42	−36.78	−40.00	−30.89	−38.07	−38.21	−38.13	−37.41	−31.70	
	Reverse	16.50	48.60	95.52	136.61	51.05	45.48	114.24	111.85	76.76	121.40	53.20	103.42	91.01	95.80	87.32	32.90	
	S/N	−24.35	−33.73	−39.60	−42.71	−34.16	−33.16	−41.16	−40.97	−37.70	−41.68	−34.52	−40.29	−39.18	−39.63	8.82	−30.34	
Main cutting force, F (N)	Forward	35.35	94.54	194.04	252.00	76.70	51.39	247.41	208.79	137.83	215.16	69.39	144.94	166.53	152.84	132.84	68.77	
	S/N	−30.97	−39.51	−45.76	−48.03	−37.70	−34.22	−47.87	−46.39	−42.79	−46.66	−36.83	−43.22	−44.43	−43.68	−42.47	−36.75	
	Reverse	41.18	110.72	206.88	267.36	92.40	74.42	250.12	237.51	147.72	231.45	89.88	185.46	180.15	182.37	163.76	73.45	
	S/N	−32.29	−40.88	−46.31	−48.54	−39.31	−37.43	−47.96	−47.51	−43.39	−47.29	−39.07	−45.37	−45.11	−45.22	4.28	−37.32	
Cutting temperature, T (°C)	Forward	500	700	890	971	732	796	931	875	957	1027	958	1035	1027	1011	1070	1044	
	S/N	−53.98	−56.90	−58.99	−59.74	−57.29	−58.02	−59.38	−58.84	−59.62	−60.23	−59.63	−60.30	−60.23	−60.10	−60.59	−60.37	
	Reverse	529	735	930	1009	810	856	953	925	882	853	858	980	951	954	961	993	
	S/N	−54.47	−58.43	−59.37	−60.74	−58.38	−59.49	−59.58	−58.56	−58.91	−58.62	−58.67	−59.82	−59.56	−58.85	−59.65	−60.76	

When the cutting speed is between 94.95 m/min and 120.58 m/min, the temperature of forward turning is lower than that of reverse turning. However, when the cutting speed is between 144.44 m/min and 173.33 m/min, the temperature of forward turning is higher than that of reverse turning. The actual cutting edge of the tool is longer during reverse turning, which improves the heat dissipation conditions.

The signal-to-noise ratios (S/N) in the measurements in the cutting temperature are listed in Table B.3. The main response of the cutting temperature S/N is plotted as shown in Fig. 15. The cutting temperature of forward turning and reverse turning rises with the increase of cutting speed, feeding speed and depth of cut. In which, the forward cutting temperature is maximized affected by the cutting speed, followed by the feeding speed, and the depth of cut is minimized. The cutting temperature for the reverse cutting is mostly affected by the feeding speed, followed by the cutting speed, and then by the depth of cut.

When a chip flows out along the rake face of the tool, its bottom layer rubs intensively the rake face of the tool, thus generating a large amount of cutting heat. When the cutting speed rises, heat is not conducted to the chip interior, resulting in a significant rise of the cutting temperature [75]. Moreover, as the metal removal rate increases proportionally with the increase of cutting speed, the machine consumes more power, the cutting heat increases, and the cutting temperature rises. Similarly, the metal removal rate increases with the increase of feeding speed, yielding the cutting temperature rises. However, the unit cutting force and unit cutting power decrease with the increase of feeding speed, and the heat generated is reduced. An increase in feeding speed leads to an increase in chip thickness and more heat carried away by chips. When the depth of cut increases, the heat generated in the cutting zones also increases. However, the length of the cutting edge participating in the work increases, and the heat dissipation conditions is improved, thus the cutting temperature does not rise significantly [76,77].

4.3. Comparison of experimental results and simulation results

The cutting forces and temperatures obtained from the finite element simulation and the experimental studies for the same cutting parameters and conditions are presented in Fig. 16. As shown in Fig. 16(a)–(f), the triaxial force values obtained from the FE simulation fluctuate with time where the experimental ones remain constant. This is likely related to much longer time scales used in measurements which average the temporal readings. Also, most of the cutting forces obtained from the simulation are higher than the experimental counterparts. The simulated axial forces for the reverse turning has the minimum deviation from the experiment of 12.43%. Noise, identification of material properties, friction coefficient, mass ratio, meshing and elements, boundary conditions and fidelity of mathematical modeling, are influencing factors for these difference [39]. The comparison of the main cutting force is shown in Fig. 16(g), where the main cutting force deviations for the forward and reverse cutting are 10.59% and 6.26%, respectively.

A comparison of the cutting temperatures obtained from the finite element simulation and the experiments for the same cutting parameters are shown in Fig. 16(h). In the temperature results, the deviations of the temperature values obtained from the simulation for the forward turning and reverse turning are 6.82% and 2.93%, respectively. Microscopic surface of the tool and the comparison of the chip morphologies are shown in Fig. 17, where a crescent-shaped damage appears on the rake face near the reverse cutting edge whereas the built-up edge formation at the radius of the tool tip. Scratches appear on both the rake and flank faces and the cutting edge breakage is more severe due to higher cutting forces during reverse turning. Continuous chip generation for both the simulation and experiment are also apparent but they differ. Chip morphologies are compared in the X-axis and Z-axis views, which show that the chip formation process can be predicted by the simulation well enough. In other studies, it was demonstrated that errors of about 10% between the experimental and simulation results are acceptable [78,79]. Therefore, the thermomechanical coupled model developed in

this work can be used to reveal the forward and reverse cutting properties.

5. Conclusions

In this paper, a new cutting approach was proposed to challenge the conventional machining concept. The MDC machining scheme for turning with an optimal cutting performance have been developed based on finite element method simulations and experiments, and the main conclusions are given below.

A multidirectional turning approach was proposed to improve the machining effectiveness and save cost for the metal cutting manufacturing industry. Among the three machining schemes established, the MDT has the optimal cutting performance with the tool cutting edge angle of 115° and the end cutting edge angle of 30°.

The MDC forward and reverse cutting have demonstrated different mechanical properties. For the cutting parameters examined in this study, the main cutting force for the MDT forward turning is mainly affected by the depth of cut, while the axial force of reverse turning depends strongly on the feeding speed. The cutting temperature for the forward turning is mostly affected by the cutting speed, while the cutting temperature of the reverse turning is strongly influenced by the feeding speed. The cutting force of reverse turning is generally higher than the forward turning, and the tool is more prone to damage and scratch near the reverse cutting edge. For the experimental cutting speed range, the temperature of the reverse turning is lower than that of the forward turning at higher cutting speeds.

The obtained in this study experimental results have demonstrated a reasonable agreement with the complex FE modeling, which gives a promise that if the developed 3D simulation model is carefully calibrated, it can be used to predict the dynamic behaviour of the MDT. This calibration will involve the process physics and parameters identification and a high fidelity numerical modeling where an optimal meshing plays a vital role. Modelling has to be continuously improved by considering effects of other MDC process and material parameters.

CRediT authorship contribution statement

Wei Cai: Conceptualization, Methodology, Writing – original draft, Writing – review & editing. **Yuanhui Zhang:** Data curation, Methodology, Writing – original draft, Writing – review & editing. **Li Li:** Writing – review & editing. **Tao Peng:** Writing – review & editing, Visualization. **Kee-hung Lai:** Writing – review & editing. **Marian Wiercigroch:** Writing – review & editing, Methodology.

Declaration of Competing Interest

The authors declare that they have no known competing financial interests or personal relationships that could have appeared to influence the work reported in this paper.

Data availability

No data was used for the research described in the article.

Acknowledgments

This work was partially supported by Sichuan Science and Technology Program (23MZGC0052), the General Research Fund of Hong Kong Research Grant Council (PolyU15500721), National Natural Science Foundation of China (No. 51875480).

Appendix A

A.1.

The average values of cutting force, cutting temperature and cutting stress for each scheme are calculated by following equation:

$$\begin{bmatrix} F_{ai} \\ T_{ai} \\ S_{ai} \end{bmatrix} = \begin{bmatrix} F^{Fi} & \left|F^{Ri}\right| \\ T^{Fi} & T^{Ri} \\ S^{Fi} & S^{Ri} \end{bmatrix} \times \begin{bmatrix} 1/2 \\ 1/2 \\ 1/2 \end{bmatrix}, i = 1, 2, 3 \tag{A.1}$$

where F_{ai} and T_{ai} are the average cutting force value and average cutting temperature of the ith scheme, respectively, F^{Fi} and T^{Fi} are the forward cutting force value and forward cutting temperature of the ith scheme, respectively, and F^{Ri} and T^{Ri} are the reverse cutting force and reverse cutting temperature value of the ith schemes, respectively, S_{ai} is the average stress of the ith scheme, S^{Fi} is the forward cutting stress of the ith scheme, S^{Ri} is the reverse cutting stress of the ith scheme.

A.2.

The difference between the results of forward turning and reverse turning is expressed by Q_I. When Q_I is positive, the result of reverse turning is higher than that of forward turning, and when the result is negative, the result of reverse turning is smaller than that of forward turning. Q_I is calculated by the following equation:

$$\begin{aligned} Q_I^F &= \frac{\left|F^R\right| - F^F}{F^F} \\ Q_I^T &= \frac{\left|T^R\right| - T^F}{T^F} \end{aligned} \tag{A.2}$$

where Q_I^F is the difference of cutting force; and Q_I^T is the difference of cutting temperature, F^F and F^R are the forward cutting force and reverse cutting force, respectively, T^R and T^F are the forward cutting temperature and reverse cutting temperature, respectively.

A.3.

The deviation of the simulation result from the experimental results is calculated by following equation:

$$\begin{aligned} \varepsilon_D^F &= \frac{|F_e - F_s|}{F_e} \\ \varepsilon_D^T &= \frac{|T_e - T_s|}{T_e} \end{aligned} \tag{A.3}$$

where ε_D^F is the deviation of cutting force; and ε_D^T is the deviation of cutting temperature, F_e and F_s are the experimental cutting force and simulation cutting force, respectively, T_e and T_s are the experimental cutting temperature and simulation cutting temperature, respectively.

Appendix B

References

[1] Chen Y, Wang J, An Q. Mechanisms and predictive force models for machining with rake face textured cutting tools under orthogonal cutting conditions. Int J Mech Sci 2021;195:106246.
[2] Cai W, Wang L, Li L, et al. A review on methods of energy performance improvement towards sustainable manufacturing from perspectives of energy monitoring, evaluation, optimization and benchmarking. Renew Sustain Energy Rev 2022;159:112227.
[3] Rao SK, Prasad R. Impact of 5 G technologies on industry 4.0. Wirel Pers Commun 2018;100:145–59.
[4] Wang B, Zhang J, Zhou W, et al. Chip inward curl and its influence on dimensional accuracy in groove cutting with a novel restricted contact tool. Adv Mech Eng 2016;8:168781401666574.
[5] Cai W, Lai K, Liu C, et al. Promoting sustainability of manufacturing industry through the lean energy-saving and emission-reduction strategy. Sci Total Environ 2019;665:23–32.
[6] Shizuka H, Sakai K, Yang H, et al. Difficult cutting property of NiTi alloy and its mechanism. J Manuf Mater Process 2020;4:124.
[7] Luan X, Zhang S, Chen J, et al. Energy modelling and energy saving strategy analysis of a machine tool during non-cutting status. Int J Prod Res 2019;57:4451–67.
[8] Fu Z, Chen X, Mao J, et al. An analytical force mode applied to three-dimensional turning based on a predictive machining theory. Int J Mech Sci 2018;136:94–105.
[9] Sugita N, Oshima M, Kimura K, et al. Novel drill bit with characteristic web shape for high efficiency and accuracy. CIRP Ann 2018;67:69–72.
[10] Zhang P, Du J, Zhang J, et al. A theoretical model to study the cutting force characteristics in remanufacturing turning of laser cladded coatings. Int J Adv Manuf Technol 2021;113:757–69.
[11] You C, Zhao G, Chu X, et al. Design, preparation and cutting performance of bionic cutting tools based on head microstructures of dung beetle. J Manuf Process 2020;58:129–35.
[12] Amini S, Fatemi MH, Atefi R. High speed turning of inconel 718 using ceramic and carbide cutting tools. Arab J Sci Eng 2013;39:2323–30. 2014.
[13] Shi W, Hou Y, Kong C, et al. Optimization of cutting force and temperature during Ti6Al4V/Al7050 laminate composites elliptical vibration turning. Proc Inst Mech Eng Part C J Mech Eng Sci 2019;233:5585–96.
[14] Chen T, Li S, Han B, et al. Study on cutting force and surface micro-topography of hard turning of GCr15 steel. Int J Adv Manuf Technol 2014;72:1639–45.
[15] Panzera TH, Souza PR, Rubio JCC, et al. Development of a three-component dynamometer to measure turning force. Int J Adv Manuf Technol 2011;62:913–22. 2012.
[16] Lomaeva TV, Kugultinov SD. Investigation of cutting modes effect on cutting force while machining titanium alloy BT6 (Russian State Standard GOST 19807-91). Mater Today Proc 2021;38:1307–9.
[17] Zhang C, Mu A, Wang Y, et al. Influence of turning parameters on cutting performance of ultra-high strength steel. Integr Ferroelectr 2020;209:110–8.
[18] Shah DR, Pancholi N, Gajera H, et al. Investigation of cutting temperature, cutting force and surface roughness using multi-objective optimization for turning of Ti-6Al-4 V (ELI). Mater Today Proc 2021;50:1379–88. 2022.
[19] Lucic M, Nedic B, Marusic V, et al. Numerical analysis of the temperature field in the cutting zone in continuous and discontinuous metal cutting by turning. Tehnički Vjesnik 2020;27:1486–91.
[20] Devin LM, Stahniv ME, Mazur MP. Analysis of thermobaric contact phenomena and calculation of temperature fields during finish turning of a VT1-0 titanium alloy with a cutter equipped with a diamond carbide blade. J Superhard Mater 2020;42:354–63.
[21] Elsadek AA, Gaafer AM, Mohamed SS, et al. Prediction and optimization of cutting temperature on hard-turning of AISI H13 hot work steel. SN Appl Sci 2020:2.
[22] Han J, Liu Z, Cao K, et al. Cutting temperature measurement in turning using fiber-optic multi-spectral radiation thermometry and its application in tool wear status recognition. Meas J Int Meas Confed 2022;198:111413.
[23] Cui X, Guo J. Effects of bioinspired microscopic geometry of ceramic tool surface on tool temperatures in continuous and interrupted turning. Int J Mech Sci 2019;157-158:715–25.
[24] Jayarjun Kadam B, Mahajan KA. Optimization of cutting temperature in machining of titanium alloy using response surface method, genetic algorithm and taguchi method. Mater Today Proc 2021;47:6285–90.
[25] Arun K, Navaneeth V, Prabhu S, et al. Experimental investigation of turning process parameter under several cutting conditions for duplex steels for minimization of cutting temperature. Mater Today Proc 2022;62:1917–20.
[26] Ravikanth D, Pranaviraj Reddy K, Srinivasa Murthy VS. Influence of tool geometry on cutting zone temperature during turning of aluminium alloy AA2219. Mater Today Proc 2022;62:2277–82.
[27] Wu M, Yu A, Chen Q, et al. Design of adjustable chip breaker for PCD turning tools. Int J Mech Sci 2020;172:105411.
[28] Jiang H, Ren Z, He L, et al. Forming process and evaluation of chip in machining of high-strength steel by an independent-developed microgroove turning tool. Sci Prog 1916;104. 20213685042110320-368504211032091.
[29] Cui X, Zhao B, Jiao F, et al. Formation characteristics of the chip and damage equivalent stress of the cutting tool in high-speed intermittent cutting. Int J Adv Manuf Technol 2016;91:2113–23. 2017.
[30] Mabrouki T, Courbon C, Zhang Y, et al. Some insights on the modelling of chip formation and its morphology during metal cutting operations. Comptes Rendus Mecanique 2016;344:335–54.
[31] Dong G, Zhaopeng H, Rongdi HY, et al. Study of cutting deformation in machining nickel-based alloy Inconel 718. Int J Mach Tools Manuf 2011;51:520–7.
[32] Xu Y, Wan Z, Zou P, et al. Experimental study on chip shape in ultrasonic vibration–assisted turning of 304 austenitic stainless steel. Adv Mech Eng 2019:11.
[33] Limin S. Correlation between serrated chip formation and turning chatter in the dry turning of superalloy. Ferroelectrics 2019;549:50–60.
[34] Chiappini E, Tirelli S, Albertelli P, et al. On the mechanics of chip formation in Ti–6Al–4 V turning with spindle speed variation. Int J Mach Tools Manuf 2014;77:16–26.
[35] Misaka T, Herwan J, Kano S, et al. Deep neural network-based cost function for metal cutting data assimilation. Int J Adv Manuf Technol 2020;107(1–2):385–98.
[36] Takabi B, Tajdari M, Tai BL. Numerical study of smoothed particle hydrodynamics method in orthogonal cutting simulations-Effects of damage criteria and particle density. J Manuf Process 2017;30:523–31.
[37] Sadeghifar M, Sedaghati R, Jomaa W, et al. A comprehensive review of finite element modeling of orthogonal machining process: chip formation and surface integrity predictions. Int J Adv Manuf Technol 2018;96(9–12):3747–91.
[38] Ijaz H, Zain-ul-Abdein M, Saleem W, et al. A numerical approach on parametric sensitivity analysis for an aeronautic aluminium alloy turning process. Mechanika 2016;22(2):149–55.
[39] Iynen O, Eksi AK, Akyildiz HK, et al. Real 3D turning simulation of materials with cylindrical shapes using ABAQUS/Explicit. J Br Soc Mech Sci Eng 2021;43(8).
[40] Arfaoui S, Zemzemi F, Dakhli M, et al. Optimization of hard turning process parameters using the response surface methodology and finite element simulations. Int J Adv Manuf Technol 2019;103(1–4):1279–90.
[41] Pei L, Shu X. Investigation of the turning process of the TC21 titanium alloy: experimental analysis and 3D simulation. Proc Inst Mech Eng Part E J Process Mech Eng 2021;235(2):489–98.
[42] Segebade E, Gerstenmeyer M, Zanger F, et al. Cutting Simulations Using a Commercially Available 2D/3D FEM Software for Forming. Procedia CIRP 2017;58:73–8.
[43] Setia S, Chauhan SR. Comparative analysis and optimization of FEM and RSM based regression model with experimental results for the dry turning of SiCp-Al7075 composite. Silicon 2020;13(12):4681–701. 2021.
[44] Malakizadi A, Hosseinkhani K, Mariano E, et al. Influence of friction models on FE simulation results of orthogonal cutting process. Int J Adv Manuf Technol 2016;88(9–12):3217–32. 2017.
[45] Yang J, Wang X, Kang M. Finite element simulation of surface roughness in diamond turning of spherical surfaces. J Manuf Process 2018;31:768–75.
[46] Luan X, Zhang S, Chen J, et al. Energy modelling and energy saving strategy analysis of a machine tool during non-cutting status. Int J Prod Res 2019;57(14):4451–67.
[47] Zhang Y, Cai W, He Y, et al. Forward-and-reverse multidirectional turning: a novel material removal approach for improving energy efficiency, processing efficiency and quality. Energy 2022;260:125162.
[48] Cai W, Li Y, Li L, et al. Energy saving and high efficiency production oriented forward-and-reverse multidirectional turning: energy modeling and application. Energy 2022;252:123981.
[49] Pham T, Nguyen D, Banh T, et al. Experimental study on the chip morphology, tool-chip contact length, workpiece vibration, and surface roughness during high-speed face milling of A6061 aluminum alloy. Proc Inst Mech Eng Part B J Eng Manuf 2020;234(3):610–20.
[50] Zhang X, Yu T, Dai Y, et al. Energy consumption considering tool wear and optimization of cutting parameters in micro milling process. Int J Mech Sci 2020;178:105628.
[51] Li T, Shi T, Tang Z, et al. Temperature monitoring of the tool-chip interface for PCBN tools using built-in thin-film thermocouples in turning of titanium alloy. J Mater Process Technol 2020;275:116376.
[52] Ji J, Huang Y, Lee K. A hybrid method based on macro-micro modeling and infrared imaging for tool temperature reconstruction in dry turning. IEEE/ASME Trans Mechatron 2018;23:1019–27.
[53] Gok A. A new approach to minimization of the surface roughness and cutting force via fuzzy TOPSIS, multi-objective grey design and RSA. Meas J Int Meas Confed 2015;70:100–9.

[54] Li Z, Fu X, Li C, et al. Modeling of instantaneous cutting force for large pitch screw with vibration consideration of the machine tool. Int J Adv Manuf Technol 2020; 108:3893–904.
[55] He Y, Zhang J, Qi Y, et al. Numerical study of microstructural effects on chip formation in high speed cutting of ductile iron with discrete element method. J Mater Process Technol 2017;249:291–301.
[56] Chinchanikar S, Choudhury SK. Machining of hardened steel—Experimental investigations, performance modeling and cooling techniques: a review. Int J Mach Tools Manuf 2015;89:95–109.
[57] Liu BX, Fan KY, Yin FX, et al. Effect of caliber rolling reduction ratios on the microstructure and mechanical properties of 45 medium carbon steel. Mater Sci Eng A Struct Mater Prop Microstruct Process 2020;774:138954.
[58] Li X, Wang R, Xin Z, et al. Changes in surface roughness and microstructure of 45 carbon steel after irradiation by electron beam. Mater Lett 2021;296:129934.
[59] Jomaa W, Mechri O, Lévesque J, et al. Finite element simulation and analysis of serrated chip formation during high–speed machining of AA7075–T651 alloy. J Manuf Process 2017;26:446–58.
[60] Duan C, Zhang L. A reliable method for predicting serrated chip formation in high-speed cutting: analysis and experimental verification. Int J Adv Manuf Technol 2012;64(9–12):1587–97. 2013.
[61] Kumar CS, Zeman P, Polcar T. A 2D finite element approach for predicting the cutting performance of nanolayered TiAlCrN coating on WC-Co cutting tool during dry turning of AISI 1045 carbon steel. Ceram Int 2020;46(16):25073–88.
[62] Saleem W, Zain-ul-abdein M, Ijaz H, et al. Computational analysis and artificial neural network optimization of dry turning parameters-AA2024-T351. Appl Sci 2017;7(6):642.
[63] Zein H, Irfan OM. Surface roughness investigation and stress modeling by finite element on orthogonal cutting of copper. Metals 2018;8(6):418 (Basel).
[64] Norouzifard V, Hamedi M. Experimental determination of the tool–chip thermal contact conductance in machining process. Int J Mach Tools Manuf 2014;84: 45–57.
[65] Atlati S, Haddag B, Nouari M, et al. Thermomechanical modelling of the tool–workmaterial interface in machining and its implementation using the ABAQUS VUINTER subroutine. Int J Mech Sci 2014;87:102–17.
[66] Wu C, Fang T, Wei Y. Effects of tool rake angle and workpiece surface roughness on nanocutting of cu investigated using Multiscale simulation. Mol Simul 2021;47: 1010–6.
[67] Cepero-Mejías F, Curiel-Sosa JL, Zhang C, et al. Effect of cutter geometry on machining induced damage in orthogonal cutting of UD polymer composites: FE study. Compos Struct 2019;214:439–50.
[68] Nobel C, Hofmann U, Klocke F, et al. Experimental investigation of chip formation, flow, and breakage in free orthogonal cutting of copper-zinc alloys. Int J Adv Manuf Technol 2016;84:1127–40. 2015.
[69] Buchkremer S, Klocke F, Lung D. Finite-element-analysis of the relationship between chip geometry and stress triaxiality distribution in the chip breakage location of metal cutting operations. Simul Modell Pract Theory 2015;55:10–26.
[70] Yue D, Zhang A, Yue C, et al. Optimization method of tool parameters and cutting parameters considering dynamic change of performance indicators. Materials 2021;14:6181 (Basel).
[71] Obiko JO, Mwema FM, Bodunrin MO. Validation and optimization of cutting parameters for Ti-6Al-4 V turning operation using DEFORM 3D simulations and Taguchi method. Manuf Rev 2021;8:5.
[72] Lalwani DI, Mehta NK, Jain PK. Experimental investigations of cutting parameters influence on cutting forces and surface roughness in finish hard turning of MDN250 steel. J Mater Process Technol 2008;206:167–79.
[73] Sivaraman V, Sankaran S, Vijayaraghavan L. A study on the influence of cutting parameters on forces during machining the multiphase V-microalloyed steel. Int J Adv Manuf Technol 2015;79:1285–92.
[74] Cao P, Zhu Z, Buck D, et al. Effect of rake angle on cutting performance during machining of stone-plastic composite material with polycrystalline diamond cutters. J Mech Sci Technol 2019;33:351–6.
[75] Hao G, Liu Z. Experimental study on the formation of TCR and thermal behavior of hard machining using TiAlN coated tools. Int J Heat Mass Transf 2019;140:1–11.
[76] Abdelnasser E, Barakat A, Elsanabary S, et al. Precision hard turning of Ti6Al4V using polycrystalline diamond inserts: surface quality, cutting temperature and productivity in conventional and high-speed machining. Materials 2020;13:5677 (Basel).
[77] Danish M, Ginta TL, Habib K, et al. Thermal analysis during turning of AZ31 magnesium alloy under dry and cryogenic conditions. Int J Adv Manuf Technol 2017;91:2855–68.
[78] Li C, Piao Y, Hu Y, et al. Modelling and experimental investigation of temperature field during fly-cutting of KDP crystals. Int J Mech Sci 2021;210:106751.
[79] Iynen O, Eksi AK, Ozdemir M, et al. Experimental and numerical investigation of cutting forces during turning of cylindrical AISI 4340 steel specimens. Materialprüfung, 2021;63:402–10.